

The role of electron correlations in the electronic structure of putative Chern magnet TbMn_6Sn_6 using correlated methods

Abdulgani Annaberdiyev¹, Lubos Mitas², Jaron T. Krogel³, and Panchapakesan Ganesh¹

1) *Center for Nanophase Materials Sciences Division,*

*Oak Ridge National Laboratory,
Oak Ridge, Tennessee 37831, USA*

2) *Department of Physics,
North Carolina State University, Raleigh,
North Carolina 27695-8202, USA*

3) *Materials Science and Technology Division,
Oak Ridge National Laboratory,
Oak Ridge, Tennessee 37831, USA*

A member of the RMn_6Sn_6 rare-earth family materials, TbMn_6Sn_6 , recently showed experimental signatures of the realization of a quantum-limit Chern magnet. Despite the promising experimental results, theoretical studies with accurate electron correlations which probe these observations have been lacking. In this work, we use quantum Monte Carlo (QMC) and density functional theory with Hubbard U (DFT+ U) calculations to examine the electronic structure of TbMn_6Sn_6 . To do so, we optimize accurate, correlation-consistent pseudopotentials for Tb and Sn using coupled-cluster and configuration-interaction (CI) methods. We find that DFT+ U and single-reference QMC calculations suffer from the same overestimation of the magnetic moments as meta-GGA and hybrid density functional approximations. Our findings point to the need for improved orbitals/wavefunctions for this class of materials, such as natural orbitals from CI, or for the inclusion of multi-reference effects that capture the static correlations for an accurate prediction of magnetic properties. The necessity for multi-reference treatment is motivated by extrapolating the dynamic correlations to the exact limit. DFT+ U with Mn magnetic moments adjusted to experiment predict the Dirac crossing in bulk to be close to the Fermi level, within ~ 120 meV, in agreement with the experiments. Our non-stoichiometric slab calculations show that the Dirac crossing approaches even closer to the Fermi level, suggesting the possible realization of Chern magnetism in this limit.

I. INTRODUCTION

Rare-earth (R) material class RMn_6Sn_6 displays rich and intricate physical phenomena consisting of strong electron-electron correlations, spin-orbit effects, and supposedly topological behavior [1–10]. These materials belong to the $P6/mmm$ (#191) space group, where Mn atoms form 2D kagome layers interlaced with R and Sn layers, see Figure 1. Although RMn_6Sn_6 family of materials has been studied for more than three decades, recent experimental anomalous Hall effect (AHE) studies [1, 9, 11] inspired a new wave of research [2–8, 12–16] on related materials.

Experimental studies show that stable compounds form for $\text{R} = \{\text{Sc}, \text{Y}, \text{Gd}, \text{Tb}, \text{Dy}, \text{Ho}, \text{Er}, \text{Tm}, \text{Yb}, \text{Lu}\}$ [17–24]. In this study, $\text{R} = \text{Tb}$ is of particular interest since it is the only element of the previous set that forms an out-of-plane spin system. In contrast, other R-element materials display either an in-plane or canted spin direction behavior [1, 2, 8, 17, 22, 23]. In particular, this case is interesting because the Chern magnetic phase predicted by Haldane’s model requires an out-of-plane spin alignment [25]. Initially, Haldane considered a honeycomb lattice [25]; however, the model was later extended to kagome systems [26]. Therefore, the kagome lattice with out-of-plane spin alignment requirement seems to be met by Mn atoms of TbMn_6Sn_6 and therefore opens

the possibility of realizing a Chern magnet in this material.

Indeed, a few years ago, Yin et al. [1] carried out experimental transport measurements using scanning tunneling microscopy (STM) in high-magnetic fields and observed a series of Landau quantization states in TbMn_6Sn_6 . They conducted AHE measurements and observed a large intrinsic contribution due to the large Berry curvature of Chern-gapped Dirac fermions. Further edge-state conductivity measurements showed significant signals within the Chern gap energy scale. Therefore, they concluded that TbMn_6Sn_6 is close to realizing a quantum-limit Chern magnet, as predicted by the Haldane model. Indeed, kagome lattice geometry with an out-of-plane magnetization formed by the Mn atoms and the presence of strong spin-orbit coupling (SOC) stemming from the Tb and Sn atoms to open a Chern gap seems to suggest that TbMn_6Sn_6 could realize such an exotic phase.

However, the possibility of realizing the Chern phase hinges on the ability to align the Fermi level (E_F) in the Dirac crossing (DC), or the Chern gap, seen in the kagome systems [1, 2, 26]. Yin and coworkers’ experiments show that the Chern gap is located at 130(4) meV above E_F [1]. However, Lee and coworkers reported density functional theory with Hubbard U (DFT+ U) calculations [2] predicting the DC to be 700 meV above E_F , or at least 300 meV above E_F , suggesting that the Dirac

crossing cannot be related to the observed AHE signal. Therefore, there seems to be a disagreement in the literature about the exact position of DC with respect to E_F and whether TbMn_6Sn_6 could realize a Chern phase. In this work, we focus on whether the DC is indeed close to the Fermi level using quantum Monte Carlo (QMC), DFT+ U , and other correlated methods.

Clearly, accurately estimating the energetic level of DC with respect to E_F , which is on the order of a few hundred meV, would require a very accurate electronic structure treatment. Such a small energetic level could be affected by the accuracy of pseudopotentials [27], the level of electron correlation treatment, the accuracy of SOC effects, and the degree of multi-reference character intrinsic to the true electronic wave function of the system. In the following sections, we thoroughly investigate these aspects and try to enumerate their contributions and biases.

In Section II, we optimize the required Tb and Sn element pseudopotentials using correlated methods and evaluate their errors via transferability tests. Then in Section III, we carry out nearly-exact energy calculations for related molecular systems to estimate the biases present in single-reference QMC calculations. We then apply the developed pseudopotentials to TbMn_6Sn_6 using DFT+ U in Section IV and QMC in Section V and demonstrate the issues with single-reference calculations. Section VI includes additional DFT+ U results, which elucidate the position of DC. The findings are further analyzed and discussed in Section VII.

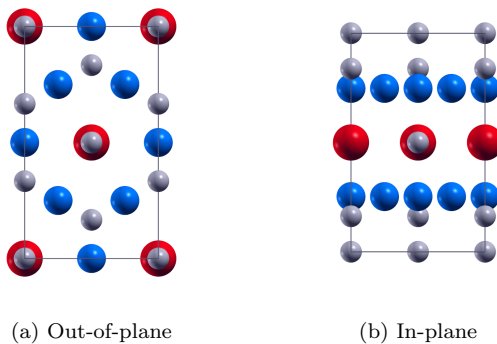


FIG. 1: A supercell of TbMn_6Sn_6 . (a) Out-of-plane and (b) in-plane views are shown. The large red spheres are Tb atoms, medium blue spheres are Mn atoms, and small gray spheres are Sn atoms.

II. PSEUDOPOTENTIALS

One of the major approximations used in correlated methods is the pseudopotential or effective core potential (ECP) approximation [28]. High-accuracy correlated methods such as configuration interaction (CI) or coupled cluster (CC) are limited by the accuracy of the ECP as

it modifies the Hamiltonian. Therefore, it's crucial that ECPs must be optimized in a correlation-consistent way, especially for correlated methods and systems. Here, we develop correlation-consistent ECPs (ccECP) for Sn and Tb elements using CC and CI methods and use a ccECP for Mn from a previously published work [29]. In the next subsections, we show the results for these elements and compare their accuracy against fully correlated, relativistic, all-electron (AE) calculations. Optimization methods and details are provided in Appendix A.

A. Sn ccECP

Figure 2 shows the Sn atomic spectrum errors for the developed ccECP and various other core approximations with respect to scalar-relativistic AE CCSD(T) data. The plot illustrates the mean absolute deviation (MAD) of a large set of energy gaps, the MAD of low-lying states (LMAD), and a weighted MAD (WMAD), which weights the gaps inverse-proportionally (see Appendix A for details). Previously tabulated ECPs - LANL2 [30], MDFSTU [31], MWBSTU [32], SDFSTU [33], BFD [34], TN-DF [35, 36], CRENBS [37], SBKJC [38], and their errors are also shown for comparison with ccECP. Here UC stands for uncorrelated core, an AE calculation with the core excitations frozen.

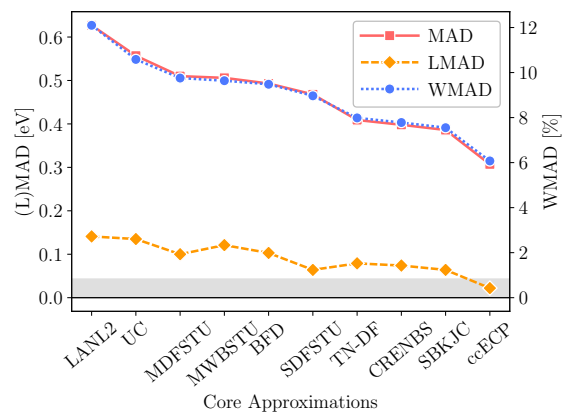


FIG. 2: Sn atom scalar relativistic AE gap (W/L)MADs for various core approximations. The shaded region represents the chemical accuracy, 1 kcal/mol (≈ 0.043 eV). UCCSD(T) method with uncontracted aug-cc-pVQZ basis set was used.

In Figure 3, transferability tests are shown using SnH and SnO molecules. Overall, the developed ccECP displays very little error, both in molecular binding and atomic gaps. Optimization of spin-orbit terms and more details of the Sn ccECP can be found in Appendix A.

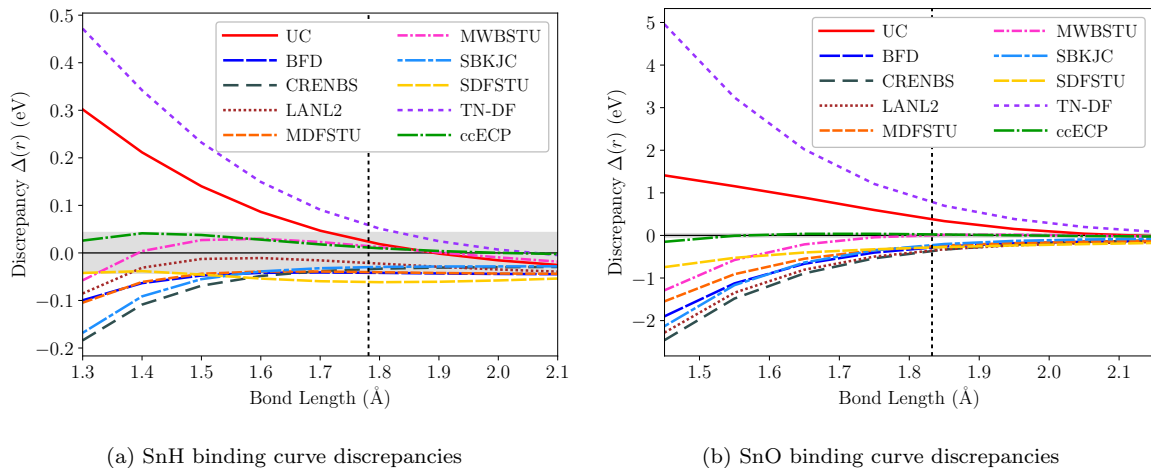


FIG. 3: Binding energy discrepancies for (a) SnH and (b) SnO molecules relative to scalar relativistic (DKH) AE UCCSD(T). The shaded region indicates the band of chemical accuracy. The dashed vertical line represents the equilibrium geometry.

B. Tb ccECP

Optimization of a Tb ECP is more involved than the case of Sn. In Sn, the electrons can be easily partitioned by quantum principle number n into core and valence spaces by treating $n \geq 5$ in the valence space ($5s$, $5p$, $5d$, ...). However, in Tb, core \leftrightarrow valence partitioning is not straightforward since $4f$ orbital eigenvalues are on the same order as $n = 5$ principal number orbitals ($5s$, $5p$, $5d$), suggesting it should be included in the valence space, see Tables 7 and 8 in the Appendix A 3. To overcome this, one could include the whole $n = 4$ electrons in the valence and treat only $n \leq 3$ electrons as the core; however, this results in a prohibitively high computational cost in many-body QMC calculations. On the other extreme, $4f$ electrons are sometimes included in the core, but this can result in poor results [27]. In this work, we decided to include the $4f$ electrons in the valence (with $N_{core} = 46 e^-$) and treat them fully self-consistently along with $5s$, $5p$, $5d$, and $6s$ orbitals. However, the many-body accuracy of such partitioning is not well-known and must therefore be carefully tested. At least in $3d$ transition metals, similar large-core ECPs with valence spaces of $3d^k 4s^2$ are well-known to produce inaccurate results [39–41]. These potentials are similar to our Tb core choice in the sense that the lowest n orbital is not an s orbital.

Our extensive many-body calculations show that the chosen core choice for Tb ccECP should result in small errors once properly optimized. In fact, the accuracy of Tb ccECP is on par with the all-electron UC where $N_{core} = 46$ electrons are not active. This is illustrated by the atomic gap errors in Figure 4 and TbH₃ and TbO molecular binding energy errors in Figure 5.

We observed that all atomic gap errors are below ~ 0.07 eV up to the third ionization potential level, see Table 9 in the Appendix A 3. Higher-order ionizations result in significantly larger errors on the order of an eV, show-

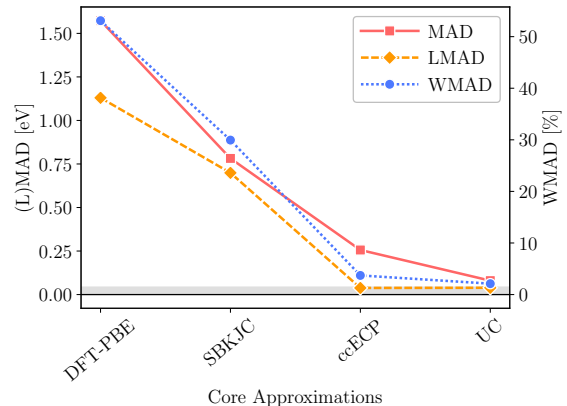


FIG. 4: Tb atom scalar relativistic AE gap (W/L)MADs for various core approximations. “DFT-PBE” is an ECP generated using the OPIUM code with a scalar-relativistic PBE and Troullier-Martins scheme.

ing the limits of such an ECP. On the other hand, very high ionization potential errors are probably not relevant for condensed matter applications since rare-earth elements form either R^{2+} or R^{3+} compounds [42]. Nevertheless, Tb ccECP is much more accurate than the existing ECPs with the same core choices, such as SBKJC [43] and an OPIUM-generated DFT-PBE [44] ECP using the Troullier-Martins scheme [45]. In fact, the ccECP errors are below chemical accuracy for the low-lying states (Figure 4) and most of the bond lengths in hydride and oxide molecules (Figure 5). The accuracy of spin-orbit terms and more details of the Tb ccECP can be found in Appendix A 3. Tb and Sn ccECPs are available online in Ref [46] for broader use.

The presented low biases of Tb and Sn ccECPs here and of Mn ccECP elsewhere [29] provide the opportunity to focus on the other systematic biases, such as the

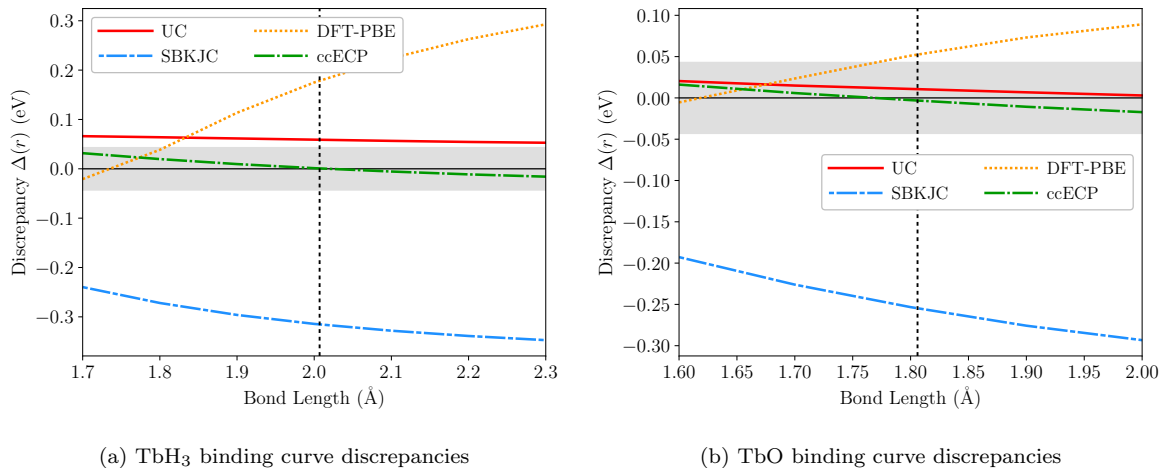


FIG. 5: Binding energy discrepancies for (a) TbH_3 and (b) TbO molecules relative to scalar relativistic (DKH) AE UCCSD(T). The shaded region indicates the band of chemical accuracy. The dashed vertical line represents the equilibrium geometry. In TbH_3 , only the bond lengths are varied while the H–Tb–H angles of 120° are kept constant. The Tb atomic energy reference is $[\text{Xe}] 4f^8 6s^2 5d^1$ state.

accuracy of the wavefunction and correlation treatment. Namely, we can assume that any deviations from the experiments are not due to the technical limitations of the representative Hamiltonians, rather it has to be due to more fundamental reasons, such as inaccurate trial wave function in QMC or improper density functional approximation (DFA) and Hubbard U in DFT+ U . These are the subjects of Sections III and IV, respectively.

III. QMC BIASES OF ELEMENTAL SUB-SPECIES

It is beneficial to know the inherent systematic biases of single-reference QMC calculations for the system of interest by comparing the QMC energies to CI or CCSD(T) energies at the complete basis set limit (CBS). Although CI and CCSD(T) calculations have been recently applied with great success to periodic systems [47–53], they are still out of reach for large systems such as TbMn_6Sn_6 [48, 53]. Therefore, we focus on constituent atoms and relevant molecular systems to estimate the QMC biases. Once the ECPs are made accurate, and other systematic errors such as timestep bias and walker population biases are under control, the main remaining errors are fixed-node and localization bias (if a nonlocal ECP is used as here). Usually, the fixed-node bias is the dominant of these two [54–56]; however, both of them go to zero as the trial wave function approaches the exact form [55, 57, 58].

We enumerate the biases of fixed-node diffusion Monte Carlo (DMC) [57] η as a percentage of the correlation energies in Figure 6 using nearly-exact energies from CCSD(T) at CBS, and single-reference DMC calculations with PBE [59], PBE0 [60], and Hartree-Fock (HF) references. This plot reveals a few insights about TbMn_6Sn_6

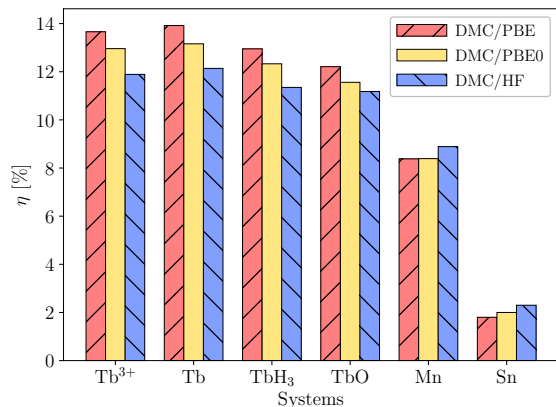


FIG. 6: Estimation of combined FN and localization biases in single-reference DMC calculations for TbMn_6Sn_6 relevant systems. Here η represents the missing percentage of the correlation energy in such calculations,

$$\eta = (E_{\text{exact}} - E_{\text{DMC}}) / (E_{\text{exact}} - E_{\text{ROHF}}) \cdot 100\%.$$

solid. First, the Sn atom has the smallest fixed-node bias, $\sim 2\%$ of the correlation energy. This error is close to the 1–2% errors of the iso-valent Si atom, Si_xH_y molecules, and diamond-structure bulk Si observed before [61, 62]. Second, Mn shows a sizable error, $\sim 9\%$ of the correlation energy missing in single-reference calculations, which also agrees with previous work [63]. Finally, the largest errors occur for systems with Tb, where $\sim 12\%$ of the correlation energy is missing. However, we found that these large biases tend to cancel out for Tb when considering energy differences, such as binding energies of TbH_3 and TbO molecules, see Table 1. In TbH_3 , the SCF binding energies (HF, PBE0, PBE) show significant variation, but DMC produces the correct D_e irrespective

of the reference trial wave function. An even larger range of SCF predictions can be seen in TbO, and DMC values are again in proximity with each other and with overall $0.15 - 0.35$ eV (2.0% – 4.5%) underestimation of D_e . This shows that the TbO trial wave function needs to be improved; nevertheless, the agreement is satisfactory, especially when PBE is used to generate the single-reference trial wavefunction for DMC.

TABLE 1: Binding energies D_e [eV] of TbH_3 and TbO without the zero-point-energy (ZPE) contributions. HF, PBE0, PBE, and DMC values using these references are shown. UCCSD(T) value is in CBS limit and can be considered the exact value. DMC and UCCSD(T) energies for O atom were obtained from Ref. [63].

Method	TbH_3	TbO
HF	6.17	4.04
PBE0	8.52	7.26
PBE	8.62	8.10
DMC/HF	8.30(1)	7.19(2)
DMC/PBE0	8.29(2)	7.32(2)
DMC/PBE	8.31(1)	7.38(2)
UCCSD(T)	8.34	7.53

In TbMn_6Sn_6 , the leading Tb atomic density of states (DOS) is well below the Fermi level (E_F), and Mn atomic DOS is dominant near E_F as shown in Figure 7. Given that the Sn atom DMC errors are small and Tb states are well below E_F , we argue that the largest errors in QMC will stem from an improper characterization of Mn atoms in our trial wave functions. In other words, low-lying conduction states near E_F might give rise to wave functions of multi-reference character due to sizable single-reference DMC error in the Mn atom. This is supported by calculated atomic moments from DFT+ U , which show severe sensitivity when U is applied on Mn- $3d$ orbitals (shown later) and insensitivity on Tb- $4f$, Tb- $5d$, and Sn- $5p$ orbitals, see Table 15 in Appendix B. In addition, we observe no changes in the band structure when + U is applied on Tb- $4f$ orbitals (Figure 16, in Appendix B).

Another insight from Figure 6 is that for a given magnetization, Tb systems with HF reference result in the lowest energies signifying the importance of localization in $4f$ orbitals. On the other hand, Mn and Sn seem to favor more delocalized orbitals when compared to HF for constrained magnetization. These aspects will be discussed later in detail by means of applying Hubbard U on Mn- $3d$ orbitals.

IV. DFA SENSITIVITY PROBLEM

This work uses the DFT+ U approach with an effective Hubbard repulsion ($U_{eff} = U - J$) [64, 65] with the fully localized limit (FLL) double counting scheme

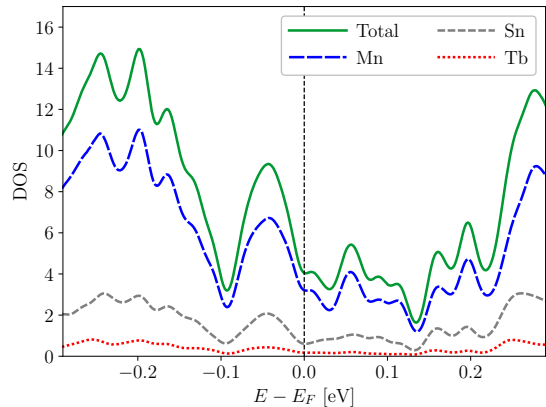


FIG. 7: Density of states of bulk TbMn_6Sn_6 . Note that Mn atomic states dominate in this small energy window while Tb states are minimal.

[65–68] as implemented in QUANTUM ESPRESSO code [69–71]. We explored two types of DFT+ U calculations. In one case, the total magnetization of the cell was constrained to agree with the experimentally observed value of $\sim M^s = 7 \mu_B$ in the SCF procedure (indicated with C-DFT, such as C-LDA or C-PBE). In the other case, the total magnetization was unconstrained and determined during the SCF cycles (simply indicated with the DFA name, such as LDA or PBE). Extended details of the employed DFT+ U methodology are given in Appendix B.

TbMn_6Sn_6 ground state is a ferrimagnetic phase (FiM), where the Mn atoms align ferromagnetically, and the Tb spins point in the opposite direction [23]. Figure 8 shows the bulk band structures using various DFAs for the FiM phase. For a pure 2D kagome lattice, tight binding models show that the DC occurs at E_F , $k = \text{K}$ point while the flat bands are above the E_F [1, 26]. Considering the LDA [72] band structure (Fig. 8a), we can see the expected “flat” bands at ~ 0.5 eV and a few DCs at ~ 0.2 eV, $k = \text{K}$. When LDA is switched to PBE DFA (Fig. 8b), these flat bands and DCs shift up by around 200 meV. Introducing a small effective Hubbard $U_{Mn}^{3d} = 0.5$ eV to LDA (Fig. 8c) shifts the flat bands and DCs up even further. Obviously, this energetic sensitivity is a problem where one is interested in resolving an energy scale of ~ 150 meV.

Another related issue is demonstrated in Figure 9 by considering the Mn magnetic moment and cell magnetization as U_{Mn}^{3d} is varied. Strikingly, the magnetizations are severely overestimated compared to the experimental green-shaded region once a small positive value of U_{Mn}^{3d} is introduced. In fact, the overestimation of magnetic moments with advanced DFAs or DFT+ U is a well-known issue for metals displaying itinerant magnetism [2, 73–75]. Previous studies [73, 74] showed that increasingly advanced DFAs in Jacob’s ladder of DFA ranks [76] such as GGA PBE [59], meta-GGA SCAN [77], and hybrid

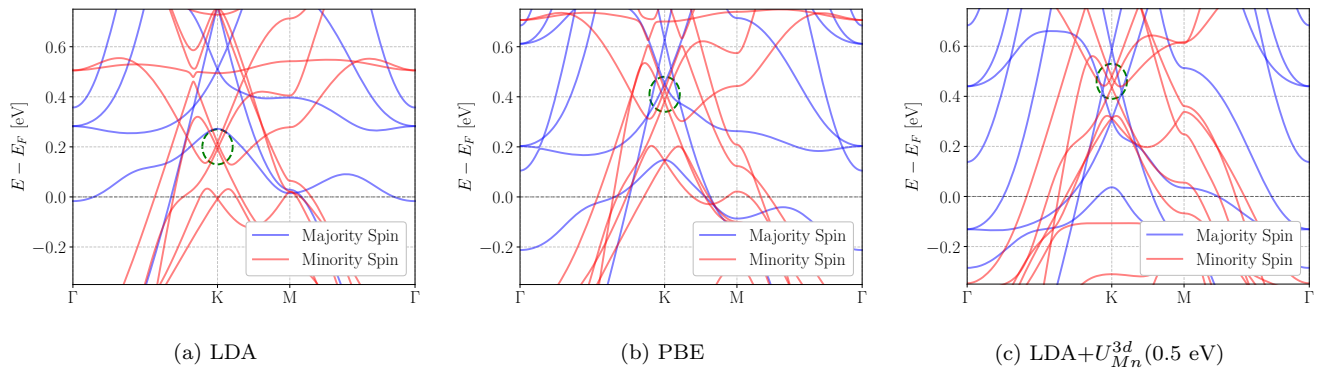


FIG. 8: Band structures of TbMn_6Sn_6 using scalar relativistic (averaged spin-orbit) ECPs. DFAs employed here are (a) LDA, (b) PBE, (c) LDA with $+U_{Mn}^{3d}$ (-0.5 eV). Note how severely DC positions (indicated by dashed green ovals) shift as the DFA is changed.

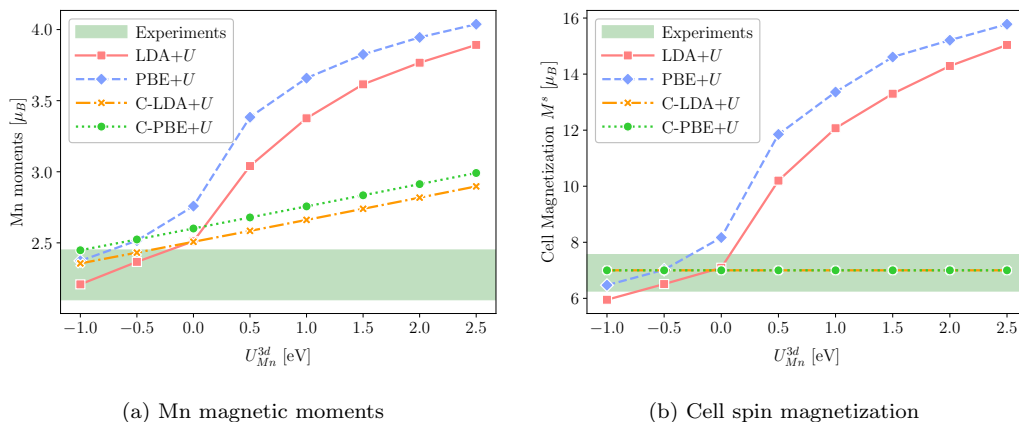


FIG. 9: Comparison of DFT+ U_{Mn}^{3d} and experimental magnetizations. (a) Mn atomic magnetic moments, (b) cell spin magnetization per formula unit. The green-shaded regions represent the envelope of various experimental measurements [1, 6, 7, 17, 19, 22, 23]. In (b), the experimental cell magnetization was added with the Tb orbital magnetization of $M_{Tb}^{orb} = 2.96 \mu_B$ [2] for a proper comparison, $M^s = M_{exp}^{total} + M_{Tb}^{orb}$.

PBE0 [60] tend to increasingly overestimate the magnetic moments in metallic ferromagnetic systems such as bcc Fe, hcp Co, and fcc Ni. Interestingly, even LDA could slightly overestimate the magnetic moments, such as in fcc Ni [74].

In Figure 9, it is evident that LDA+ U requires a small negative U_{Mn}^{3d} value to agree with both experimental Mn atomic moment and overall cell magnetization. We note that utilization of a negative U was suggested [78, 79] and applied [80–84] before, especially on superconducting systems. Physically, this means that Hund’s exchange J dominates the on-site Coulomb repulsion U , resulting in a minor negative $U_{eff} = U - J$ value. The result is more delocalization of orbitals and a tendency to pair electrons which produce lower magnetic moments. The opposite extreme can be seen when using HF and hybrid DFA for metals, which over-localize the electrons and tend to unpair the electrons resulting in overestimated magnetic moments. Even though DFT+($U > 0$) physics is different than hybrid DFAs, the effect is a similar localization

of orbitals [78]. In this case, the proper delocalization could be achieved by a minor negative U_{eff} or a Hund’s J with a magnitude larger than U . In addition, previous studies showed that the employed double-counting scheme in DFT+ U could significantly change the predicted magnetic moments [2, 85]. Ultimately, the key goal is to achieve a proper (de)localization of electrons and hence correct magnetization driven by an appropriate tendency of electrons to pair. The difficulties of predicting magnetic moments using advanced DFAs beg the question, “can single-reference QMC calculations predict the correct magnetization in a complex correlated metal such as TbMn_6Sn_6 ”?

V. SINGLE-REFERENCE QMC

In order to assess the validity of single-reference QMC, we consider results from two different QMC methods. These methods are fixed-node DMC (captures

most correlations), and $\sigma^2 \rightarrow 0$ extrapolated VMC ($\text{VMC}_{\text{extrap}}^{\sigma^2 \rightarrow 0}$, full correlation limit) using single-reference Slater-Jastrow type trial wave functions. As kinetic energy sampling via k -mesh integration is crucial in metals [86–89], we use canonical twist-averaging (CTA) and a supercell with two formula units (Figure 1) in all TbMn_6Sn_6 QMC calculations. Extended details of QMC methods are given in Appendix C

The $\text{VMC}_{\text{extrap}}^{\sigma^2 \rightarrow 0}$ method uses two data points with the same determinantal form to extrapolate to the $\sigma^2 = 0$ limit. Specifically, energies from the Slater trial wave function and Slater-Jastrow trial wave function with one-, two-, and three-body terms (SJ_{123}) were used in the extrapolation. In principle, as the variance goes to zero, the VMC energy should recover the exact correlation energy due to zero-variance principal [57]. However, since the Jastrow factor only captures the dynamic correlations [90], this estimator will only reach the exact dynamic correlation limit, with static correlations remaining unrecovered due to missing multi-determinant form. Such an extrapolation is illustrated in Figure 10 for the TbO molecule, where we have access to nearly-exact energies from $\text{UCCSD(T)}/\text{CBS}$. Even though $\text{VMC}_{\text{extrap}}^{\sigma^2 \rightarrow 0}$ estimator energy is below the single-reference DMC, it is still significantly above the exact energy since the estimator is not capturing the static correlations due to single-reference form. We observed similar plots with the same energy ordering for the other molecules considered in this work; see Appendix C for all Figures. The only exception to this was the Sn atom, where the $\text{VMC}_{\text{extrap}}^{\sigma^2 \rightarrow 0}$ estimated energy goes slightly below the $\text{UCCSD(T)}/\text{CBS}$ value.

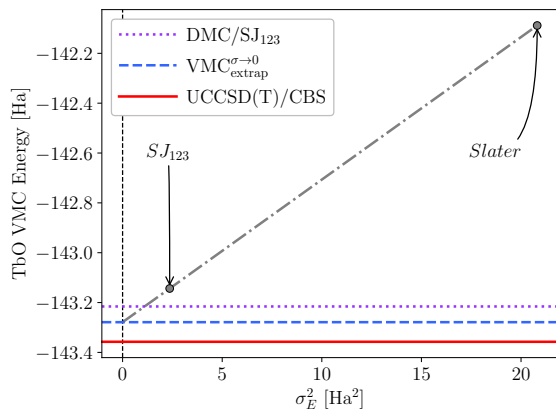


FIG. 10: VMC energy vs. variance extrapolation for TbO molecule. $\text{DMC}/\text{SJ}_{123}$ is a DMC calculation using Slater-Jastrow form with one-, two-, and three-body terms in the Jastrow. $\text{UCCSD(T)}/\text{CBS}$ represents the nearly-exact energy from basis set extrapolations. Note that the extrapolated VMC energy obtains lower energy than $\text{DMC}/\text{SJ}_{123}$; however, it is still above the exact energy due to missing static correlations.

In Figure 11, we plot the bulk energies with the above-described methods where the orbitals are generated from

$\text{DFA} = \{\text{LDA}, \text{PBE}\}$. Specifically, LDA DFT calculations obtain magnetizations close to the experiments, so it is interesting to see whether QMC predicts the correct magnetization when the LDA orbitals are reused for various QMC magnetizations. Namely, in Figure 11, the same orbitals are used, but a different overall magnetization M^s is constructed in QMC calculations. Since QMC methods are variational, the lowest energy states correspond to the physical predictions from single reference QMC. As shown in these plots, the lowest energy for both estimators corresponds to $\sim 15 \mu_B$, approximately twice the correct value and well outside of the experimental region. This overestimation seems independent of the employed orbitals, as LDA and PBE results follow similar trends. In addition, extrapolating the dynamic correlations to the exact limit does not change the energy curve, signifying a necessity for either significantly improved orbitals or including static correlations via multi-reference wavefunctions.

Next, we explore fixing the QMC cell magnetization to agree with experiments (at $M^s = 7 \mu_B$) and varying the orbitals by the introduction of Hubbard $+U$ (Figure 12). In Figures 12a, 12b this is done for unconstrained DFT (M^s from SCF) and magnetization-constrained DFT ($M^s = 7 \mu_B$) using an effective Hubbard U as described in Section IV. In Figure 12a, the DMC method obtains the lowest energy for unconstrained LDA at $U_{Mn}^{3d} = 1 \text{ eV}$. The magnetization in this reference is severely overestimated in DFT with cell magnetization of $\approx 12 \mu_B$ and Mn moment of $3.38 \mu_B$, see Figure 9. On the other hand, the lowest DMC energy for the constrained reference occurs at a much larger value of $U_{Mn}^{3d} = 2 \text{ eV}$. This is because in the constrained case, the Mn moments increase much more slowly as U_{Mn}^{3d} is increased (Figure 9a) requiring a larger value of U_{Mn}^{3d} . This suggests that the magnetization of Mn atoms dictates the QMC energy.

In Figure 12b, similar plots are shown using $\text{VMC}_{\text{extrap}}^{\sigma^2 \rightarrow 0}$ method. The results are qualitatively similar to DMC in Figure 12a, but the minima are shifted by about $\Delta U_{Mn}^{3d} = 0.5 \text{ eV}$ closer to zero. However, the corresponding DFT magnetizations are still considerably overestimated and outside the experimental measurements. This shows that including the full dynamic correlations can improve the prediction of magnetic properties, but it is not enough for an accurate estimation in this case.

Finally, we explored the effect of J in the $\text{DFT}+U+J$ formalism [68] in Figures 12c, 12d. We consider LDA with $U_{Mn}^{3d} = 1.0 \text{ eV}$, which results in the lowest energy in DMC for this DFA (Figure 12a). In $\text{DMC}/\text{SJ}_{123}$ method, Figure 12c, the energies increase as J is increased. This is because the effect of J is to discourage high-spin states, and we see a similar effect as in Figure 12a. The $\text{VMC}_{\text{extrap}}^{\sigma^2 \rightarrow 0}$ in Figure 12c method predicts a value of $J_{Mn}^{3d} = 0.6 \text{ eV}$; however, the corresponding Mn moment of $2.61 \mu_B$ is still slightly overestimated relative to the experimental value of $2.39(8) \mu_B$ [23] (see Figure 19 in the Appendix B).

It is evident from Figure 12 that constraining the QMC

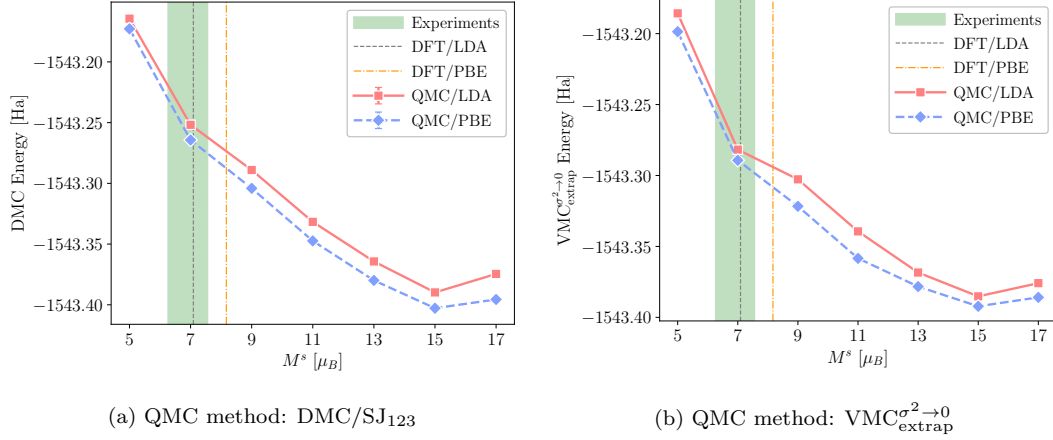


FIG. 11: QMC energies [Ha] using LDA and PBE trial wave functions for various QMC magnetizations M^s . The green-shaded regions represent the envelope of various experimental measurements [1, 6, 7, 17, 19, 22, 23]. The experimental cell magnetization was added with the Tb orbital magnetization of $M_{Tb}^{orb} = 2.96 \mu_B$ [2] for a proper comparison, $M^s = M_{exp}^{total} + M_{Tb}^{orb}$. DFT-predicted magnetizations are also shown as vertical lines.

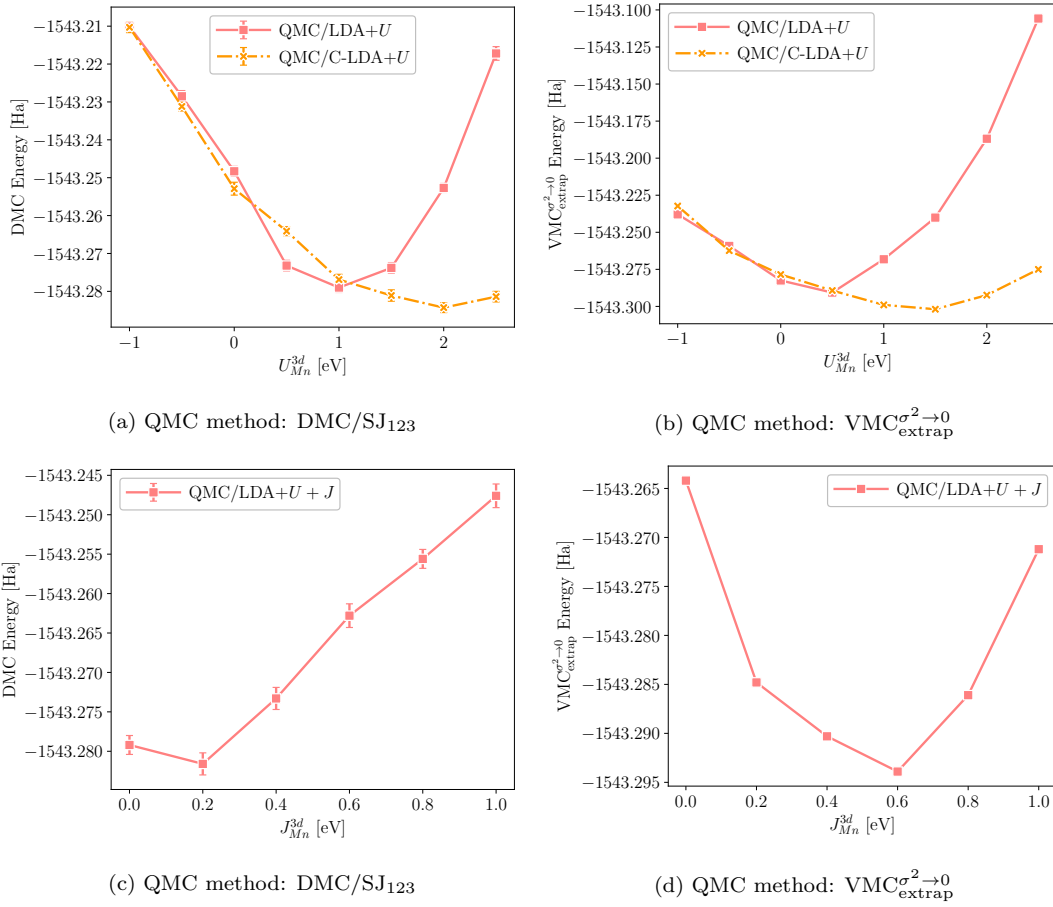


FIG. 12: QMC energies [Ha] using (a, b) $DFT+U_{eff}$ [64, 65] and (c, d) $DFT+U+J$ [68] trial wave functions. The QMC spins are constrained at $M^s = N_e^{up} - N_e^{down} = 7 \mu_B$ for each twist.

cell magnetization seems to alleviate the overestimation problem. This is especially pronounced in the $\text{VMC}_{\text{extrap}}^{\sigma \rightarrow 0}$ case with exact dynamic correlations. However, the lowest energies using constrained QMC cell magnetizations in Figure 12 are still much higher than the unrestricted, $M^s = 15 \mu_B$ case in Figure 11. This is true within each method, DMC/SJ₁₂₃ and $\text{VMC}_{\text{extrap}}^{\sigma \rightarrow 0}$. Intuitively, the QMC overestimation issue could be explained as follows. Mn element in the atomic limit favors the ${}^6S_{5/2}$ high-spin state [91], and this localized atomic energy scale could dominate the QMC energy in the metallic solid. The energy due to bonding is partially captured in the single-reference case; however, it is not properly balanced with the localized energy scale, which skews the optimal energy to the Mn atomic high-spin state. Therefore, a balanced trial wave function would also need to capture the multi-reference effects stemming from crystal field and orbital hybridization so as to counterweight the pronounced atomic high-spin limit. Indeed, in the HF method, where there are no correlations by definition, the Mn moment is close to the fully unpaired limit of $5 \mu_B$, see Table 2. Compared to insulators, the interactions must be significantly screened in metals [92], and HF or hybrid DFAs are well-known to result in poor screening [93, 94], and other unphysical features in partially-filled band metals [95, 96]. We note that in the thermodynamic limit (TDL) of full-CI (FCI), the proper screening must be achieved in metallic systems due to the cancellation of static correlation effects and long-range interactions [94–97]. Remarkably, the approximate correlations in LDA seem to effectively capture the screening and multi-reference effects quite well, judging by the obtained magnetizations in Table 2. In addition, a few previous studies found that LDA could account for the long-range correlations due to multireference effects [98, 99].

TABLE 2: Mn moments and cell magnetizations M^s for various DFAs. The fraction of exact exchange (EXX) in the DFAs is shown. Note that as EXX is increased, the magnetizations are increasingly overestimated.

DFA	EXX	Mn [μ_B]	M^s [μ_B]
LDA	0.00	2.51	7.09
PBE	0.00	2.76	8.17
B3LYP	0.20	3.38	10.81
PBE0	0.25	3.47	11.00
HF	1.00	4.34	14.09
Exp. [7, 23]		2.39(8)	6.86

The presented calculations show that single-reference QMC overestimates the magnetic moments similar to meta-GGA SCAN and hybrid PBE0 DFAs. This overestimation trend persists even when the dynamic correlations are extrapolated to the exact values, Figure 11. This points to a significant deficiency in static correlations, which possibly stem from a few sources:

1. Imperfect one-particle orbitals. Within the single-

reference framework, the nodal surface is fully determined by the single-particle inputs. In case of the presence of static/multi-reference correlations, this can bias the expectations. Natural orbitals (NOs) from CI calculations can provide a better orbital set for improving the description within the single-reference model [100].

2. Lack of multi-reference trial wave function. Even with high-quality orbitals such as NOs, it is possible that multi-reference wave functions are needed to predict the magnetic moments correctly. This would not be surprising because systems with Mn elements are known to display multi-reference characters [101]. For instance, a previous study of bulk MnO using CCSD found improvement in band gaps and magnetic moments on the overestimated values of UHF [53].

An additional example where a similar problem occurs is the W atom. Its ground state is $[\text{Xe}]4f^{14}5d^46s^2$ (5D) configuration, while the first excited state configuration is a higher spin $[\text{Xe}]4f^{14}5d^56s^1$ (7S) [91]. Fixed-phase spin-orbit DMC, with minimal expansion of determinants, incorrectly predicts the high-spin state 7S as the ground state [102]. However, as the trial wave function is expanded with more determinants, the correct 5D ground state is recovered in agreement with the experiments [102].

3. Finite-size effects. In this work, we used a supercell with two formula units and canonical twist-averaging where each twist is occupied with the same M^s . Although CTA should reach the same TDL energy as grand-canonical twist averaging (GCTA) for the same magnetization, it could have a considerable impact on finite supercell sizes. This overlaps with the first point above as it is a one-body effect. However, it has a different origin since the change is across-twist rather than within-twist.

Although the above effects can be present, it is out of the scope of this work to study TDL convergence and to apply multi-reference approaches here since we are interested in the single-reference model and its accuracy limit for these types of materials. Therefore, we leave these aspects for future study. However, in order to shed additional light on the intricate relationship of single-reference and magnetic order, we empirically adjust the magnetic moment of the Mn atom to an experimental result of $2.39(8) \mu_B$ [23]. Most recent experimental measurements also obtained an Mn moment of $\sim 2.4 \mu_B$ at low temperatures [6]. We note that using the Mn moments as a reference is more robust than comparing against the overall cell magnetization or Tb atomic moments due to the orbital magnetic moment contribution of the localized and well-screened $4f$ orbitals [42]. On the other hand, the $3d$ orbital magnetic moments are negligible due to orbital quenching [2, 42] and the spin

moments can be directly compared with the experiments. We find that employing LDA DFA, a small effective value $U_{Mn}^{3d} \approx -0.5$ eV is required to match with the neutron diffraction experimental value of $2.39(8) \mu_B$ [23]. This is corroborated by Figure 6, where Mn seems to favor more delocalized orbitals for the given magnetization, and previous studies showing that even LDA, which presumably produces the smallest orbital localization, shows a tendency to overestimate the magnetic moments [73, 74].

VI. DFT+U RESULTS

Having established an appropriate DFA for the study of TbMn_6Sn_6 , we now plot the bulk band structure using $\text{LDA}+U_{Mn}^{3d}$ with $U_{Mn}^{3d} = -0.5$ eV. In Figure 13a, the bands are plotted with scalar relativistic pseudopotentials, namely, with averaged spin-orbit interactions. We find that the DC energetic level (E_{DC}) with respect to E_F shifts down to about $E_{DC} = 120$ meV when compared with LDA. This is in excellent agreement with the experimental result of $E_{DC}^{exp} = 130(4)$ meV from tunneling and quasiparticle scattering along the bulk crystal edge direction [1]. In addition, the inclusion of explicit SOC results in the opening of the Chern gap in the DCs seen at 120 meV above E_F , Figure 13c. The Chern gap here is $\Delta = 25$ meV, which is also in reasonable agreement with the experimental value of $\Delta^{exp} = 34(2)$ meV. Therefore, our results are in partial disagreement with those of Ref. [2], where the DC was estimated to be too high, 300 – 700 meV above the E_F .

Our calculations show the DC in bulk is close to E_F , which could affect the experimental AHE measurements. An important distinction between the bulk theory and experimental transport measurements is that the experiments were carried out in a cleaved bulk terminated with an Mn surface. The Mn termination could further modify the band structure near the surface. To explore this, we carried out DFT+ U calculations of a $\text{TbMn}_{12}\text{Sn}_{10}$ non-stoichiometric semi-infinite slab terminated with Mn layers. In other words, the slab is periodic along in-plane directions, while a large vacuum is inserted in both out-of-plane ends, which are terminated with Mn layers, see Figure 14. To demonstrate that the Mn surface effects can be appropriately modeled by this slab, we calculated the atomic moments and charges in these two settings. Table 3 provides these values for Tb and Mn in various environments. We observed that the Tb spin moments and charges are largely unchanged for bulk vs. slab, indicating that the relevant changes occur only in the surface and sub-surface Mn layers as well as Sn layers in between. The sub-surface Mn shows a moderate change in the moments. However, a significant change occurs near the Mn surface, where we see much larger Mn moments of $3.33 \mu_B$, in quantitative agreement with previous findings [2]. This shows that the surface effects can be reliably modeled by the constructed slab.

Figure 13b and 13d show the slab band structures. As

TABLE 3: Comparison of atomic moments and charges in bulk vs. slab. Scalar-relativistic $\text{LDA}+U_{Mn}^{3d}(-0.5$ eV) results. Note that Tb quantities are very close, signifying that slab calculation is a good model for the Mn-surface cleaved bulk.

Atom	Environment	Moment [μ_B]	Charge [e^-]
Tb	Slab	-6.41	1.17
Tb	Bulk	-6.40	1.18
Mn	Slab surface	3.33	1.48
Mn	Slab subsurface	2.32	1.43
Mn	Bulk	2.37	1.44

we can see, the DC has shifted down even closer to E_F . In Figure 13a, where the SOC is not explicitly included, the DC is ~ 15 meV below the E_F . However, once the SOC is included, the Chern gap of $\Delta = 26$ meV opens up, and the Fermi level lies within this gap. In reality, the Fermi level in the cleaved bulk might or might not exactly lie in the Chern gap of $34(2)$ meV, as the *ab-initio* methods used here combined with a level of experimental input could result in larger systematic biases than 34 meV. However, the change in E_{DC} going from the bulk to the surface, $\Delta E_{DC} = 135$ meV must be a more robust quantity, as this is an energy difference, and we expect it to be much less sensitive to the quality of DFA or trial wave functions.

In order to obtain further insights into the DC's origin, we investigated their orbital characters using projections onto the atomic Mn orbitals. There are two DCs near 120 meV in bulk (Figure 13). One of these has a heavy d_{zx} and d_{zy} character, while the other has a d_{xy} and $d_{x^2-y^2}$ character (see Figure 20 in the Appendix). When looking at surface and subsurface Mn layers, the DC at ~ 120 meV with d_{zx} , d_{zy} character can no longer be seen near the E_F (see Figures 21 and 22 in the Appendix). Therefore, we focus on DC with d_{xy} , $d_{x^2-y^2}$ character and plot the projected band structures of the surface, subsurface, and bulk Mn layers in Figure 15. The subsurface Mn bands look similar to the bulk Mn bands, but the DC appears closer to E_F . On the other hand, the surface bands look quite different, and the d_{xy} , $d_{x^2-y^2}$ DC signal near the E_F is very weak. We note that a DC near E_F can still be seen on the surface Mn layer, albeit with strong d_{z^2} , d_{zx} , and d_{zy} characters (Figure 22 in Appendix B). Namely, the DC near E_F in the slab (Figure 13b) is split between the surface and subsurface DCs in the d -orbital manifold with different characters. Perhaps it is not surprising that the surface DC takes on a substantial z character since it now faces the vacuum. Assuming that STM transport measurements involved conduction mainly in x , y directions (in-plane), the above DC split suggests that the experimental signal mainly consists of the bulk and subsurface layers with a stronger d_{xy} , $d_{x^2-y^2}$ character, and a weaker signal coming from the surface Mn d_{zx} , d_{zy} orbitals. This is corroborated by the fact that the STM Landau fan di-

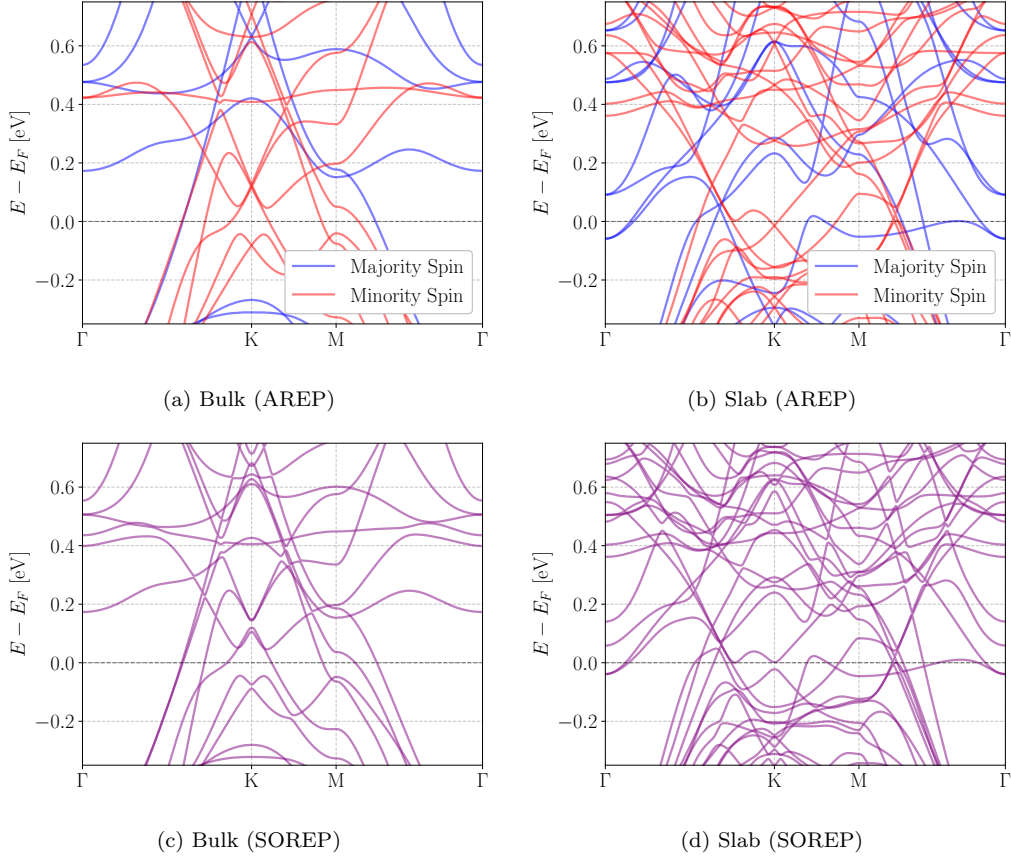


FIG. 13: Band structures of TbMn_6Sn_6 bulk using $\text{LDA}+U_{Mn}^{3d}(-0.5 \text{ eV})$. (a) Scalar relativistic (averaged spin-orbit coupling), (b) fully relativistic (explicit spin-orbit coupling).

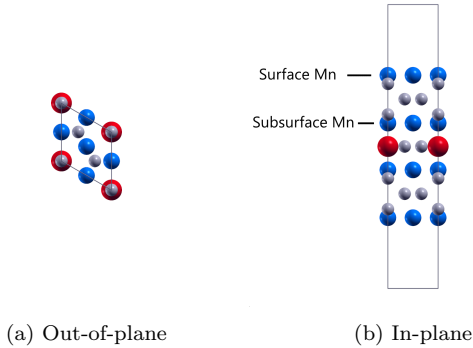


FIG. 14: A slab of TbMn_6Sn_6 . (a) Out-of-plane and (b) in-plane views are shown. The large red spheres are Tb atoms, medium blue spheres are Mn atoms, and small gray spheres are Sn atoms. The vacuum length between the periodic slabs is $\approx 13.5 \text{ \AA}$.

agram obtained from an Mn-terminated bulk shows the Chern gap at $130(4) \text{ meV}$ above E_F , not near E_F as we see for the surface.

Another aspect of this material studied by Ref. [2] was the k_z dispersion of the bulk TbMn_6Sn_6 . Specifically, the

authors mentioned that the k_z -dispersion was too high in the bulk TbMn_6Sn_6 , which is not desired for a 2D model. Indeed, we also find this to be true in bulk, and the band structure shows drastic changes as the k_z is slowly varied (Figure 23 in Appendix B). In fact, the DC occurs only in $k_z = 0$ when looked at increments of $\Delta k_z = 0.1$ in reciprocal lattice units and disappears for higher values. The “flat” band in $k_z = 0$ also gradually disperses for high k_z values. The non-ideal 2D nature of the bulk can be seen in the Fermi surface as well (see Figure 24 in Appendix B). This demonstrates the additional challenge in realizing the Chern magnetism in the bulk Mn layers and motivates the experimental synthesis of TbMn_6Sn_6 thin films to eliminate the heavy k_z -dependence and to move the DC closer to E_F .

VII. CONCLUSIONS

This study has made advancements in three distinct but related directions. First, an accurate, correlation-consistent ECP was generated for the Tb element with a valence space of $4f^9 5s^2 5p^6 6s^2$. To the best of our knowledge, the accuracy of such a core-valence partitioning was not known for many-body methods such as CCSD(T) or

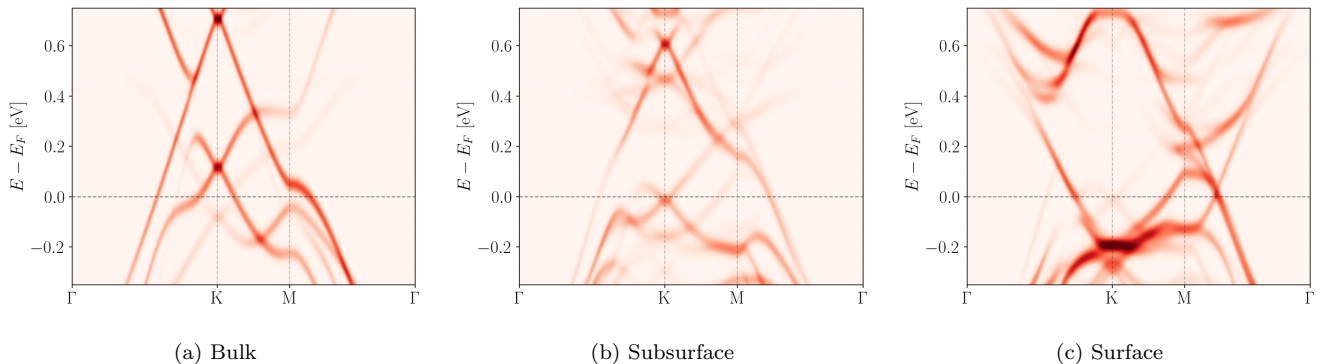


FIG. 15: Minority spin band structures using projections on the atomic Mn ($d_{xy} + d_{x^2-y^2}$) orbitals.

DMC. In CCSD(T), we found that the low-lying atomic gaps and the binding energies of TbH_3 and TbO can be made chemically accurate (1 kcal/mol) with careful optimizations. In the light of obtained results, this seemingly too technical aspect of the effective core model is actually important for a clear delineation of subtle physical effects in the studied system. Single-reference DMC calculations showed that $\approx 12\%$ of the correlation energy is missing in Tb, TbH_3 , and TbO . We believe the promising results obtained for the Tb element indicate that similarly accurate ccECPs could be generated for other rare-earth elements. Such a set of rare-earth ccECPs would open new possibilities to study the broader family of RMn_6Sn_6 with significantly improved accuracy using many-body methods such as CCSD(T), CI, QMC, and also DFT with appropriate DFAs. In fact, the current progress in applying real-space QMC to f -element systems seems to be hindered by the unavailability of accurate enough rare-earth ECPs, as we were able to find only a few QMC studies in the literature [103–106]. Therefore, we hope this work will motivate new studies in this avenue.

Second, recent studies [73, 74] showed that meta-GGA such as SCAN, hybrid DFT such as PBE0, and DFT+ U methods overestimate the magnetic moments in simple elemental metals such as bcc Fe, hcp Co, fcc Ni, and other transition metals. Here we observe a similar overestimation in Mn magnetic moments when using DFT+ U . Importantly, we show that single-reference QMC calculations also severely overestimate the transition metal moments similar to the previously shown [73, 74] advanced DFAs such as SCAN and PBE0. The overestimation persists even when the dynamic correlations are extrapolated to the exact limit suggesting that a multi-reference treatment is needed to predict the magnetic moments correctly. These results have broader implications for the ability of commonly used DFAs, such as LDA, to effectively capture the multi-reference effects and for the origins of effective weak interactions in metallic systems. A study of static correlation effects is possible for such systems with small primitive cells as multi-reference methods such as CCSD(T) and CI mature for use in periodic boundary conditions. We leave this aspect of the

study to future work and hope that these findings will stimulate further research in this direction.

Finally, using a combination of *ab-initio* and neutron diffraction experimental results, we reveal key insights about TbMn_6Sn_6 bulk and non-stoichiometric thin film limit. We show that DC is only ~ 120 meV above E_F in bulk, in agreement with experiments [1] and in partial disagreement with a previous DFT+ U study [2]. However, the realization of Chern magnetism in bulk is complicated by the heavy k_z -dispersion as suggested previously [2, 7]. We show that in the slab, the DC shifts even closer to E_F . This motivates further experimental studies of TbMn_6Sn_6 in the thin film limit to eliminate the k_z -dispersion and to probe for the possible realization of Chern magnetism. Viable pathways to experimentally synthesize these thin films and whether they can be formed in a thermodynamically stable, defect-free way [107] remains to be shown. Our work thus illuminates the aspects of TbMn_6Sn_6 both from theoretical and experimental viewpoints and opens the door for future studies of this exciting material.

VIII. DATA AVAILABILITY

See the Appendix for detailed information on the calculations, such as pseudopotential optimization (Appendix A), DFT+ U methods and data (Appendix B), QMC methods and data (Appendix C), and employed bulk and slab geometries (Appendix D). The input files, output files, and supporting data generated in this work are published in Materials Data Facility [108, 109] and can be found in Ref. [110].

The Department of Energy will provide public access to these results of federally sponsored research in accordance with the DOE Public Access Plan (<http://energy.gov/downloads/doe-public-access-plan>).

ACKNOWLEDGMENTS

We thank P. R. C. Kent and Anand Bhattacharya for reading the manuscript and providing helpful suggestions.

This work has been supported by the U.S. Department of Energy, Office of Science, Basic Energy Sciences, Materials Sciences and Engineering Division, as part of the Computational Materials Sciences Program and Center for Predictive Simulation of Functional Materials.

An award of computer time was provided by the Innovative and Novel Computational Impact on Theory and Experiment (INCITE) program. This research used resources of the Oak Ridge Leadership Computing Facility, which is a DOE Office of Science User Facility supported under Contract No. DE-AC05-00OR22725. This research used resources of the National Energy Research Scientific Computing Center (NERSC), a U.S. Depart-

ment of Energy Office of Science User Facility located at Lawrence Berkeley National Laboratory, operated under Contract No. DE-AC02-05CH11231.

This paper describes objective technical results and analysis. Any subjective views or opinions that might be expressed in the paper do not necessarily represent the views of the U.S. Department of Energy or the United States Government.

This manuscript has been authored by UT-Battelle, LLC under Contract No. DE-AC05-00OR22725 with the U.S. Department of Energy. The United States Government retains and the publisher, by accepting the article for publication, acknowledges that the United States Government retains a non-exclusive, paid-up, irrevocable, world-wide license to publish or reproduce the published form of this manuscript, or allow others to do so, for United States Government purposes.

-
- [1] Jia-Xin Yin, Wenlong Ma, Tyler A. Cochran, Xitong Xu, Songtian S. Zhang, Hung-Ju Tien, Nana Shumiya, Guangming Cheng, Kun Jiang, Biao Lian, Zhida Song, Guoqing Chang, Ilya Belopolski, Daniel Multer, Maksim Litskevich, Zi-Jia Cheng, Xian P. Yang, Bianca Swidler, Huibin Zhou, Hsin Lin, Titus Neupert, Ziqiang Wang, Nan Yao, Tay-Rong Chang, Shuang Jia, and M. Zahid Hasan. Quantum-limit Chern topological magnetism in TbMn_6Sn_6 . *Nature*, 583(7817):533–536, July 2020.
- [2] Y. Lee, R. Skomski, X. Wang, P. P. Orth, A. K. Pathak, B. N. Harmon, R. J. McQueeney, I. I. Mazin, and Liqin Ke. Interplay between magnetism and band topology in Kagome magnets RMn_6Sn_6 , April 2022.
- [3] Xitong Xu, Jia-Xin Yin, Wenlong Ma, Hung-Ju Tien, Xiao-Bin Qiang, P. V. Sreenivasa Reddy, Huibin Zhou, Jie Shen, Hai-Zhou Lu, Tay-Rong Chang, Zhe Qu, and Shuang Jia. Topological charge-entropy scaling in kagome Chern magnet TbMn_6Sn_6 . *Nature Communications*, 13(1):1197, March 2022.
- [4] Christopher Sims. Evolution of the Chern Gap in Kagome Magnet $\text{HoMn}_6\text{Sn}_{6-x}\text{Ge}_x$. *Condensed Matter*, 7(2):40, June 2022.
- [5] S. X. M. Riberolles, Tyler J. Slade, D. L. Abernathy, G. E. Granroth, Bing Li, Y. Lee, P. C. Canfield, B. G. Ueland, Liqin Ke, and R. J. McQueeney. Low-Temperature Competing Magnetic Energy Scales in the Topological Ferrimagnet TbMn_6Sn_6 . *Physical Review X*, 12(2):021043, May 2022.
- [6] C. Mielke III, W. L. Ma, V. Pomjakushin, O. Zaharko, S. Sturniolo, X. Liu, V. Ukleev, J. S. White, J.-X. Yin, S. S. Tsirkin, C. B. Larsen, T. A. Cochran, M. Medarde, V. Porée, D. Das, R. Gupta, C. N. Wang, J. Chang, Z. Q. Wang, R. Khasanov, T. Neupert, A. Amato, L. Liborio, S. Jia, M. Z. Hasan, H. Luetkens, and Z. Guguchia. Low-temperature magnetic crossover in the topological kagome magnet TbMn_6Sn_6 . *Communications Physics*, 5(1):1–9, May 2022.
- [7] D. Connor Jones, Suvadip Das, Hari Bhandari, Xiaoxiong Liu, Peter Siegfried, Madhav P. Ghimire, Stepan S. Tsirkin, I. I. Mazin, and Nirmal J. Ghimire. Origin of spin reorientation and intrinsic anomalous Hall effect in the kagome ferrimagnet TbMn_6Sn_6 , March 2022.
- [8] Wenlong Ma, Xitong Xu, Jia-Xin Yin, Hui Yang, Huibin Zhou, Zi-Jia Cheng, Yuqing Huang, Zhe Qu, Fa Wang, M. Zahid Hasan, and Shuang Jia. Rare Earth Engineering in RMn_6Sn_6 ($R = \text{Gd}-\text{Tm}, \text{Lu}$) Topological Kagome Magnets. *Physical Review Letters*, 126(24):246602, June 2021.
- [9] Lingling Gao, Shiwei Shen, Qi Wang, Wujun Shi, Yi Zhao, Changhua Li, Weizheng Cao, Cuiying Pei, Jun-Yi Ge, Gang Li, Jun Li, Yulin Chen, Shichao Yan, and Yanpeng Qi. Anomalous Hall effect in ferrimagnetic metal RMn_6Sn_6 ($R = \text{Tb}, \text{Dy}, \text{Ho}$) with clean Mn kagome lattice. *Applied Physics Letters*, 119(9):092405, August 2021.
- [10] Nirmal J. Ghimire, Rebecca L. Dally, L. Poudel, D. C. Jones, D. Michel, N. Thapa Magar, M. Bleuel, Michael A. McGuire, J. S. Jiang, J. F. Mitchell, Jeffrey W. Lynn, and I. I. Mazin. Competing magnetic phases and fluctuation-driven scalar spin chirality in the kagome metal YMn_6Sn_6 . *Science Advances*, 6(51):eabe2680, December 2020.
- [11] Wenlong Ma, Xitong Xu, Zihe Wang, Huibin Zhou, Madalynn Marshall, Zhe Qu, Weiwei Xie, and Shuang Jia. Anomalous Hall effect in the distorted kagome magnets $(\text{Nd}, \text{Sm})\text{Mn}_6\text{Sn}_6$. *Physical Review B*, 103(23):235109, June 2021.
- [12] Shuting Peng, Yulei Han, Ganesh Pokharel, Jianchang Shen, Zeyu Li, Makoto Hashimoto, Donghui Lu, Brenden R. Ortiz, Yang Luo, Houchen Li, Mingyao Guo, Bingqian Wang, Shengtao Cui, Zhe Sun, Zhenhua Qiao, Stephen D. Wilson, and Junfeng He. Realizing Kagome Band Structure in Two-Dimensional Kagome Surface States of RV_6Sn_6 ($R = \text{Gd}, \text{Ho}$). *Physical Review Letters*, 127(26):266401, December 2021.
- [13] Yong Hu, Xianxin Wu, Yongqi Yang, Shunye Gao, Nicholas C. Plumb, Andreas P. Schnyder, Weiwei Xie, Junzhang Ma, and Ming Shi. Tunable topological Dirac surface states and van Hove singularities in kagome

- metal GdV_6Sn_6 . *Science Advances*, 8(38):eadd2024, September 2022.
- [14] Xi-Mei Li, Zheng-Zhe Lin, Xin-Wei Chen, and Xi Chen. Selective CO_2 reduction on topological Chern magnet TbMn_6Sn_6 . *Physical Chemistry Chemical Physics*, 24(31):18600–18607, August 2022.
- [15] Lujin Min, Milos Sretenovic, Thomas W. Heitmann, Tyler W. Valentine, Rui Zu, Venkatraman Gopalan, Christina M. Rost, Xianglin Ke, and Zhiqiang Mao. A topological kagome magnet in high entropy form. *Communications Physics*, 5(1):1–7, March 2022.
- [16] Dong Chen, Congcong Le, Chenguang Fu, Haicheng Lin, Walter Schnelle, Yan Sun, and Claudia Felser. Large anomalous Hall effect in the kagome ferromagnet LiMn_6Sn_6 . *Physical Review B*, 103(14):144410, April 2021.
- [17] S. Kimura, A. Matsuo, S. Yoshii, K. Kindo, L. Zhang, E. Brück, K.H.J. Buschow, F.R. de Boer, C. Lefevre, and G. Venturini. High-field magnetization of RMn_6Sn_6 compounds with $\text{R}=\text{Gd}$, Tb , Dy and Ho . *Journal of Alloys and Compounds*, 408–412:169–172, February 2006.
- [18] B. Malaman, G. Venturini, R. Welter, J. P. Sanchez, P. Vulliet, and E. Ressouche. Magnetic properties of RMn_6Sn_6 ($\text{R}=\text{Gd}-\text{Er}$) compounds from neutron diffraction and Mössbauer measurements. *Journal of Magnetism and Magnetic Materials*, 202(2):519–534, August 1999.
- [19] D. M. Clatterbuck and K. A. Gschneidner. Magnetic properties of RMn_6Sn_6 ($\text{R}=\text{Tb}$, Ho , Er , Tm , Lu) single crystals. *Journal of Magnetism and Magnetic Materials*, 207(1):78–94, 1999.
- [20] G. Venturini, D. Fruchart, and B. Malaman. Incommensurate magnetic structures of RMn_6Sn_6 ($\text{R} = \text{Sc}$, Y , Lu) compounds from neutron diffraction study. *Journal of Alloys and Compounds*, 236(1):102–110, April 1996.
- [21] Y. Amako, T. Yamamoto, and H. Nagai. The ^{119}Sn Mössbauer effect in RMn_6Sn_6 compounds ($\text{R}=\text{Gd}, \text{Y}$). *Hyperfine Interactions*, 94(1):1897–1901, December 1994.
- [22] G. Venturini, B. Chafik El Idrissi, and B. Malaman. Magnetic properties of RMn_6Sn_6 ($\text{R} = \text{Sc}$, Y , $\text{Gd}-\text{Tm}$, Lu) compounds with HfFe_6Ge_6 type structure. *Journal of Magnetism and Magnetic Materials*, 94(1-2):35–42, March 1991.
- [23] B. Chafik El Idrissi, G. Venturini, B. Malaman, and D. Fruchart. Magnetic structures of TbMn_6Sn_6 and HoMn_6Sn_6 compounds from neutron diffraction study. *Journal of the Less Common Metals*, 175(1):143–154, September 1991.
- [24] B. Chafik El Idrissi, G. Venturini, and B. Malaman. Refinement of HfFe_6Ge_6 isostructural ScMn_6Sn_6 and TbMn_6Sn_6 . *Materials Research Bulletin*, 26(6):431–437, June 1991.
- [25] F. D. M. Haldane. Model for a Quantum Hall Effect without Landau Levels: Condensed-Matter Realization of the "Parity Anomaly". *Physical Review Letters*, 61(18):2015–2018, October 1988.
- [26] Kenya Ohgushi, Shuichi Murakami, and Naoto Nagaosa. Spin Anisotropy and Quantum Hall Effect in the Kagome Lattice: Chiral Spin State Based on a Ferromagnet. *Physical Review B*, 62(10):R6065–R6068, September 2000.
- [27] Vinay I. Hegde, Christopher K. H. Borg, Zachary del Rosario, Yoolhee Kim, Maxwell Hutchinson, Erin Antono, Julia Ling, Paul Saxe, James E. Saal, and Bryce Meredig. Quantifying uncertainty in high-throughput density functional theory: A comparison of AFLOW, Materials Project, and OQMD, November 2022.
- [28] Michael Dolg and Xiaoyan Cao. Relativistic Pseudopotentials: Their Development and Scope of Applications. *Chemical Reviews*, 112(1):403–480, January 2012.
- [29] Benjamin Kincaid, Guangming Wang, Haihan Zhou, and Lubos Mitas. Correlation consistent effective core potentials for late 3d transition metals adapted for plane wave calculations. *The Journal of Chemical Physics*, 157(17):174307, November 2022.
- [30] P. Jeffrey Hay and Willard R. Wadt. Ab initio effective core potentials for molecular calculations. Potentials for K to Au including the outermost core orbitals. *The Journal of Chemical Physics*, 82(1):299, August 1998.
- [31] Hermann Stoll, Bernhard Metz, and Michael Dolg. Relativistic energy-consistent pseudopotentials—Recent developments. *Journal of Computational Chemistry*, 23(8):767–778, 2002.
- [32] Andreas Bergner, Michael Dolg, Wolfgang Küchle, Hermann Stoll, and Heinz Werner Preuß. Ab initio energy-adjusted pseudopotentials for elements of groups 13–17. *Molecular Physics*, 80(6):1431–1441, December 1993.
- [33] G. Igel-Mann, H. Stoll, and H. Preuss. Pseudopotentials for main group elements (IIIa through VIIa). *Molecular Physics*, 65(6):1321–1328, December 1988.
- [34] M. Burkatzki, C. Filippi, and M. Dolg. Energy-consistent pseudopotentials for quantum Monte Carlo calculations. *The Journal of Chemical Physics*, 126(23):234105, June 2007.
- [35] J. R. Trail and R. J. Needs. Smooth relativistic Hartree–Fock pseudopotentials for H to Ba and Lu to Hg . *The Journal of Chemical Physics*, 122(17):174109, May 2005.
- [36] J. R. Trail and R. J. Needs. Norm-conserving Hartree–Fock pseudopotentials and their asymptotic behavior. *The Journal of Chemical Physics*, 122(1):014112, January 2005.
- [37] L. A. LaJohn, P. A. Christiansen, R. B. Ross, T. Atashroo, and W. C. Ermler. Ab initio relativistic effective potentials with spin–orbit operators. III. Rb through Xe . *The Journal of Chemical Physics*, 87(5):2812–2824, September 1987.
- [38] Walter J. Stevens, Morris Krauss, Harold Basch, and Paul G. Jasien. Relativistic compact effective potentials and efficient, shared-exponent basis sets for the third-, fourth-, and fifth-row atoms. *Canadian Journal of Chemistry*, 70(2):612–630, February 1992.
- [39] Ji-Woo Lee, Lubos Mitas, and Lucas K. Wagner. Quantum Monte Carlo study of MnO solid, November 2004.
- [40] Jun Koseki, Ryo Maezono, Masanori Tachikawa, M. D. Towler, and R. J. Needs. Quantum Monte Carlo study of porphyrin transition metal complexes. *The Journal of Chemical Physics*, 129(8):085103, August 2008.
- [41] M. Burkatzki, Claudia Filippi, and M. Dolg. Energy-consistent small-core pseudopotentials for 3d-transition metals adapted to quantum Monte Carlo calculations. *The Journal of Chemical Physics*, 129(16):164115, October 2008.
- [42] Sam Mugiraneza and Alannah M. Hallas. Tutorial: A beginner’s guide to interpreting magnetic susceptibility data with the Curie-Weiss law. *Communications*

- Physics*, 5(1):1–12, April 2022.
- [43] Thomas R. Cundari and Walter J. Stevens. Effective core potential methods for the lanthanides. *The Journal of Chemical Physics*, 98(7):5555–5565, April 1993.
- [44] Opium - pseudopotential generation project. <https://opium.sourceforge.net/>. Accessed: 2022-10-21.
- [45] N. Troullier and José Luís Martins. Efficient pseudopotentials for plane-wave calculations. *Physical Review B*, 43(3):1993–2006, January 1991.
- [46] Pseudopotential Library: A community website for pseudopotentials/effective core potentials developed for high accuracy correlated many-body methods such as quantum Monte Carlo and quantum chemistry. <https://pseudopotentiallibrary.org>. Accessed: 2022-11-18.
- [47] Thomas Gruber, Ke Liao, Theodoros Tsatsoulis, Felix Hummel, and Andreas Grüneis. Applying the Coupled-Cluster Ansatz to Solids and Surfaces in the Thermodynamic Limit. *Physical Review X*, 8(2):021043, May 2018.
- [48] Anouar Benali, Kevin Gasperich, Kenneth D. Jordan, Thomas Applencourt, Ye Luo, M. Chandler Bennett, Jaron T. Krogel, Luke Shulenburger, Paul R. C. Kent, Pierre-François Loos, Anthony Scemama, and Michel Caffarel. Toward a systematic improvement of the fixed-node approximation in diffusion Monte Carlo for solids—A case study in diamond. *The Journal of Chemical Physics*, 153(18):184111, November 2020.
- [49] Alejandro Gallo, Felix Hummel, Andreas Irmeler, and Andreas Grüneis. A periodic equation-of-motion coupled-cluster implementation applied to F-centers in alkaline earth oxides. *The Journal of Chemical Physics*, 154(6):064106, February 2021.
- [50] Xiao Wang and Timothy C. Berkelbach. Excitons in Solids from Periodic Equation-of-Motion Coupled-Cluster Theory. *Journal of Chemical Theory and Computation*, 16(5):3095–3103, May 2020.
- [51] Tina N. Mihm, Tobias Schäfer, Sai Kumar Ramadugu, Laura Weiler, Andreas Grüneis, and James J. Shepherd. A shortcut to the thermodynamic limit for quantum many-body calculations of metals. *Nature Computational Science*, 1(12):801–808, December 2021.
- [52] Verena A. Neufeld, Hong-Zhou Ye, and Timothy C. Berkelbach. Ground-State Properties of Metallic Solids from Ab Initio Coupled-Cluster Theory. *The Journal of Physical Chemistry Letters*, 13(32):7497–7503, August 2022.
- [53] Yang Gao, Qiming Sun, Jason M. Yu, Mario Motta, James McClain, Alec F. White, Austin J. Minnich, and Garnet Kin-Lic Chan. Electronic structure of bulk manganese oxide and nickel oxide from coupled cluster theory. *Physical Review B*, 101(16):165138, April 2020.
- [54] L. Mitáš. Pseudopotential Quantum Monte Carlo for Large-Z Atom Systems. In David P. Landau, K. K. Mon, and Heinz-Bernd Schüttler, editors, *Computer Simulation Studies in Condensed-Matter Physics V*, Springer Proceedings in Physics, pages 94–105, Berlin, Heidelberg, 1993. Springer.
- [55] Jaron T. Krogel and P. R. C. Kent. Magnitude of pseudopotential localization errors in fixed node diffusion quantum Monte Carlo. *The Journal of Chemical Physics*, 146(24):244101, June 2017.
- [56] Allison L. Dzubak, Jaron T. Krogel, and Fernando A. Reboredo. Quantitative estimation of localization errors of 3d transition metal pseudopotentials in diffusion Monte Carlo. *The Journal of Chemical Physics*, 147(2):024102, July 2017.
- [57] W. M. C. Foulkes, L. Mitas, R. J. Needs, and G. Rajagopal. Quantum Monte Carlo simulations of solids. *Reviews of Modern Physics*, 73(1):33–83, January 2001.
- [58] Raymond C. Clay, Michael P. Desjarlais, and Luke Shulenburger. Deuterium Hugoniot: Pitfalls of thermodynamic sampling beyond density functional theory. *Physical Review B*, 100(7):075103, August 2019.
- [59] John P. Perdew, Kieron Burke, and Matthias Ernzerhof. Generalized Gradient Approximation Made Simple. *Physical Review Letters*, 77(18):3865–3868, October 1996.
- [60] John P. Perdew, Matthias Ernzerhof, and Kieron Burke. Rationale for mixing exact exchange with density functional approximations. *The Journal of Chemical Physics*, 105(22):9982–9985, December 1996.
- [61] Guangming Wang, Abdulgani Annaberdiyev, and Lubos Mitas. Binding and excitations in Si_xH_y molecular systems using quantum Monte Carlo. *The Journal of Chemical Physics*, 153(14):144303, October 2020.
- [62] Abdulgani Annaberdiyev, Guangming Wang, Cody A. Melton, M. Chandler Bennett, and Lubos Mitas. Cohesion and excitations of diamond-structure silicon by quantum Monte Carlo: Benchmarks and control of systematic biases. *Physical Review B*, 103(20):205206, May 2021.
- [63] Abdulgani Annaberdiyev, Cody A. Melton, M. Chandler Bennett, Guangming Wang, and Lubos Mitas. Accurate Atomic Correlation and Total Energies for Correlation Consistent Effective Core Potentials. *Journal of Chemical Theory and Computation*, 16(3):1482–1502, March 2020.
- [64] Matteo Cococcioni and Stefano de Gironcoli. Linear response approach to the calculation of the effective interaction parameters in the LDA + U method. *Physical Review B*, 71(3):035105, January 2005.
- [65] S. L. Dudarev, G. A. Botton, S. Y. Savrasov, C. J. Humphreys, and A. P. Sutton. Electron-energy-loss spectra and the structural stability of nickel oxide: An LSDA+U study. *Physical Review B*, 57(3):1505–1509, January 1998.
- [66] V. I. Anisimov, I. V. Solovyev, M. A. Korotin, M. T. Czyżyk, and G. A. Sawatzky. Density-functional theory and NiO photoemission spectra. *Physical Review B*, 48(23):16929–16934, December 1993.
- [67] Vladimir I. Anisimov, F. Aryasetiawan, and A. I. Liechtenstein. First-principles calculations of the electronic structure and spectra of strongly correlated systems: The LDA+ U method. *Journal of Physics: Condensed Matter*, 9(4):767, January 1997.
- [68] A. I. Liechtenstein, V. I. Anisimov, and J. Zaanen. Density-functional theory and strong interactions: Orbital ordering in Mott-Hubbard insulators. *Physical Review B*, 52(8):R5467–R5470, August 1995.
- [69] Paolo Giannozzi, Stefano Baroni, Nicola Bonini, Matteo Calandra, Roberto Car, Carlo Cavazzoni, Davide Ceresoli, Guido L. Chiarotti, Matteo Cococcioni, Ismaila Dabo, Andrea Dal Corso, Stefano de Gironcoli, Stefano Fabris, Guido Fratesi, Ralph Gebauer, Uwe Gerstmann, Christos Gougoussis, Anton Kokalj, Michele Lazzeri, Layla Martin-Samos, Nicola Marzari, Francesco Mauri, Riccardo Mazzarello, Stefano Paolini,

- Alfredo Pasquarello, Lorenzo Paulatto, Carlo Sbraccia, Sandro Scandolo, Gabriele Scლაუzero, Ari P. Seitsonen, Alexander Smogunov, Paolo Umari, and Renata M. Wentzcovitch. QUANTUM ESPRESSO: A modular and open-source software project for quantum simulations of materials. *Journal of Physics: Condensed Matter*, 21(39):395502, September 2009.
- [70] P. Giannozzi, O. Andreussi, T. Brumme, O. Bunau, M. Buongiorno Nardelli, M. Calandra, R. Car, C. Cavazzoni, D. Ceresoli, M. Cococcioni, N. Colonna, I. Carnimeo, A. Dal Corso, S. de Gironcoli, P. Delugas, R. A. DiStasio, A. Ferretti, A. Floris, G. Fratesi, G. Fugallo, R. Gebauer, U. Gerstmann, F. Giustino, T. Gorni, J. Jia, M. Kawamura, H.-Y. Ko, A. Kokalj, E. Küçükbenli, M. Lazzeri, M. Marsili, N. Marzari, F. Mauri, N. L. Nguyen, H.-V. Nguyen, A. Otero-de-la-Roza, L. Paulatto, S. Poncé, D. Rocca, R. Sabatini, B. Santra, M. Schlipf, A. P. Seitsonen, A. Smogunov, I. Timrov, T. Thonhauser, P. Umari, N. Vast, X. Wu, and S. Baroni. Advanced capabilities for materials modelling with Quantum ESPRESSO. *Journal of Physics: Condensed Matter*, 29(46):465901, October 2017.
- [71] Paolo Giannozzi, Oscar Basesggio, Pietro Bonfà, Davide Brunato, Roberto Car, Ivan Carnimeo, Carlo Cavazzoni, Stefano de Gironcoli, Pietro Delugas, Fabrizio Ferrari Ruffino, Andrea Ferretti, Nicola Marzari, Iurii Timrov, Andrea Urru, and Stefano Baroni. Quantum ESPRESSO toward the exascale. *The Journal of Chemical Physics*, 152(15):154105, April 2020.
- [72] J. P. Perdew and Alex Zunger. Self-interaction correction to density-functional approximations for many-electron systems. *Physical Review B*, 23(10):5048–5079, May 1981.
- [73] Yuhao Fu and David J. Singh. Applicability of the Strongly Constrained and Appropriately Normed Density Functional to Transition-Metal Magnetism. *Physical Review Letters*, 121(20):207201, November 2018.
- [74] Yuhao Fu and David J. Singh. Density functional methods for the magnetism of transition metals: SCAN in relation to other functionals. *Physical Review B*, 100(4):045126, July 2019.
- [75] Sukanya Ghosh, Soheil Ershadrad, Vladislav Borisov, and Biplab Sanyal. Unraveling effects of electron correlation in two-dimensional Fe_nGeTe_2 ($n=3, 4, 5$) by dynamical mean field theory, December 2022.
- [76] John P. Perdew and Karla Schmidt. Jacob’s ladder of density functional approximations for the exchange-correlation energy. *AIP Conference Proceedings*, 577(1):1–20, July 2001.
- [77] Jianwei Sun, Adrienn Ruzsinszky, and John P. Perdew. Strongly Constrained and Appropriately Normed Semilocal Density Functional. *Physical Review Letters*, 115(3):036402, July 2015.
- [78] Heather J. Kulik. Perspective: Treating electron overdelocalization with the DFT+U method. *The Journal of Chemical Physics*, 142(24):240901, June 2015.
- [79] M. Cococcioni. The LDA + U Approach : A Simple Hubbard Correction for Correlated Ground States. In *Correlated Electrons: From Models to Materials*, 2012.
- [80] Clas Persson and Susanne Mirbt. Improved electronic structure and optical properties of sp-hybridized semiconductors using LDA+U SIC. *Brazilian Journal of Physics*, 36:286–290, June 2006.
- [81] H. Nakamura, N. Hayashi, N. Nakai, and M. Machida. LDA + Negative U Solves a Puzzle of too Large Calculated Magnetic Moment in Iron-based Superconductor $\text{LaFeAsO}_{1-x}\text{F}_x$, June 2008.
- [82] H. Nakamura, N. Hayashi, N. Nakai, and M. Machida. First-principle calculation for the phonon structure on iron-based superconductors. *Physica C: Superconductivity*, 469(15):1024–1026, October 2009.
- [83] R. Micnas, J. Ranninger, and S. Robaszkiewicz. Superconductivity in narrow-band systems with local non-retarded attractive interactions. *Reviews of Modern Physics*, 62(1):113–171, January 1990.
- [84] Izumi Hase and Takashi Yanagisawa. Madelung energy of the valence-skipping compound BaBiO_3 . *Physical Review B*, 76(17):174103, November 2007.
- [85] Siheon Ryee and Myung Joon Han. The effect of double counting, spin density, and Hund interaction in the different DFT+U functionals. *Scientific Reports*, 8(1):9559, June 2018.
- [86] Sam Azadi and W. M. C. Foulkes. Systematic study of finite-size effects in quantum Monte Carlo calculations of real metallic systems. *The Journal of Chemical Physics*, 143(10):102807, June 2015.
- [87] Sam Azadi and W. M. C. Foulkes. Efficient method for grand-canonical twist averaging in quantum Monte Carlo calculations. *Physical Review B*, 100(24):245142, December 2019.
- [88] Mario Dagrada, Seher Karakuzu, Verónica Laura Vildosola, Michele Casula, and Sandro Sorella. Exact special twist method for quantum Monte Carlo simulations. *Physical Review B*, 94(24):245108, December 2016.
- [89] C. Lin, F. H. Zong, and D. M. Ceperley. Twist-averaged boundary conditions in continuum quantum Monte Carlo algorithms. *Physical Review E*, 64(1):016702, June 2001.
- [90] Chien-Jung Huang, C. J. Umrigar, and M. P. Nightingale. Accuracy of electronic wave functions in quantum Monte Carlo: The effect of high-order correlations. *The Journal of Chemical Physics*, 107(8):3007–3013, August 1997.
- [91] A. Kramida, Yu. Ralchenko, J. Reader, and NIST ASD Team. NIST Atomic Spectra Database (ver. 5.10), [Online]. Available: <https://physics.nist.gov/asd> [2022, December 22]. National Institute of Standards and Technology, Gaithersburg, MD., 2022.
- [92] Giuseppe Grosso and Giuseppe Pastori Parravicini. Chapter 7 - Excitons, Plasmons, and Dielectric Screening in Crystals. In Giuseppe Grosso and Giuseppe Pastori Parravicini, editors, *Solid State Physics (Second Edition)*, pages 287–331. Academic Press, Amsterdam, January 2014.
- [93] Efthimios Kaxiras. *Atomic and Electronic Structure of Solids*. Cambridge University Press, 2003.
- [94] Benjamin G. Janesko, Thomas M. Henderson, and Gustavo E. Scuseria. Screened hybrid density functionals for solid-state chemistry and physics. *Physical Chemistry Chemical Physics*, 11(3):443–454, January 2009.
- [95] Hendrik J. Monkhorst. Hartree-Fock density of states for extended systems. *Physical Review B*, 20(4):1504–1513, August 1979.
- [96] Joseph Delhalle and Jean-Louis Calais. Direct-space analysis of the Hartree-Fock energy bands and density of states for metallic extended systems. *Physical Review B*, 35(18):9460–9466, June 1987.
- [97] Subhasish Mandal, Kristjan Haule, Karin M. Rabe, and

- David Vanderbilt. Electronic correlation in nearly free electron metals with beyond-DFT methods. *npj Computational Materials*, 8(1):1–7, August 2022.
- [98] Victor Polo, Jürgen Gräfenstein, Elfi Kraka, and Dieter Cremer. Long-range and short-range Coulomb correlation effects as simulated by Hartree–Fock, local density approximation, and generalized gradient approximation exchange functionals. *Theoretical Chemistry Accounts*, 109(1):22–35, February 2003.
- [99] DIETER CREMER. Density functional theory: Coverage of dynamic and non-dynamic electron correlation effects. *Molecular Physics*, 99(23):1899–1940, December 2001.
- [100] Ting Wang, Xiaojun Zhou, and Fan Wang. Performance of the Diffusion Quantum Monte Carlo Method with a Single-Slater-Jastrow Trial Wavefunction Using Natural Orbitals and Density Functional Theory Orbitals on Atomization Energies of the Gaussian-2 Set. *The Journal of Physical Chemistry A*, 123(17):3809–3817, May 2019.
- [101] Maria Drosou, Christiana A. Mitsopoulou, and Dimitrios A. Pantazis. Spin-state energetics of manganese spin crossover complexes: Comparison of single-reference and multi-reference ab initio approaches. *Polyhedron*, 208:115399, November 2021.
- [102] Guangming Wang, Benjamin Kincaid, Haihan Zhou, Abdulgani Annaberdiyev, M. Chandler Bennett, Jaron T. Krogel, and Lubos Mitas. A new generation of effective core potentials from correlated and spin-orbit calculations: Selected heavy elements. *The Journal of Chemical Physics*, 157(5):054101, August 2022.
- [103] Nagat Elkahwagy, Atif Ismail, S M A Maize, and K R Mahmoud. Diffusion Monte Carlo Calculations for Rare-earths: Hartree-Fock, Hybrid B3LYP, and Long-range Corrected LC-BLYP Functional. *Universal Journal of Physics and Application*, page 6, 2016.
- [104] Nagat Elkahwagy, Atif Ismail, S M A Maize, and K R Mahmoud. Diffusion Monte Carlo study of actinide monohydrides and monofluorides. *Rev. Mex. Fis.*, page 6, 2017.
- [105] Nagat Elkahwagy, Atif Ismail, S. M. A. Maize, and K. R. Mahmoud. Theoretical Investigation on the Low-Lying States of LaP Molecule. *Chinese Physics Letters*, 35(10):103101, October 2018.
- [106] N. Devaux, M. Casula, F. Decremps, and S. Sorella. Electronic origin of the volume collapse in cerium. *Physical Review B*, 91(8):081101, February 2015.
- [107] Alex Zunger. Beware of plausible predictions of fantasy materials. *Nature*, 566(7745):447–449, February 2019.
- [108] B. Blaiszik, K. Chard, J. Pruyne, R. Ananthakrishnan, S. Tuecke, and I. Foster. The Materials Data Facility: Data Services to Advance Materials Science Research. *JOM*, 68(8):2045–2052, August 2016.
- [109] Ben Blaiszik, Logan Ward, Marcus Schwarting, Jonathon Gaff, Ryan Chard, Daniel Pike, Kyle Chard, and Ian Foster. A data ecosystem to support machine learning in materials science. *MRS Communications*, 9(4):1125–1133, December 2019.
- [110] Abdulgani Annaberdiyev, Lubos Mitas, Jaron T. Krogel, and Panchapakesan Ganesh. The role of electron correlations in the electronic structure of putative Chern magnet TbMn₆Sn₆ using correlated methods. <https://doi.org/10.18126/icm7-z0n8>, January 2023.
- [111] Hans-Joachim Werner, Peter J. Knowles, Gerald Knizia, Frederick R. Manby, and Martin Schütz. Molpro: A general-purpose quantum chemistry program package. *WIREs Computational Molecular Science*, 2(2):242–253, 2012.
- [112] Trond Saue, Radovan Bast, André Severo Pereira Gomes, Hans Jørgen Aa. Jensen, Lucas Visscher, Ignacio Agustín Aucar, Roberto Di Remigio, Kenneth G. Dyall, Ephraim Eliav, Elke Fasshauer, Timo Fleig, Loïc Halbert, Erik Donovan Hedegård, Benjamin Helmich-Paris, Miroslav Iliáš, Christoph R. Jacob, Stefan Knecht, Jon K. Laerdahl, Marta L. Vidal, Malaya K. Nayak, Małgorzata Olejniczak, Jógvan Magnus Haugaard Olsen, Markus Pernpointner, Bruno Senjean, Avijit Shee, Ayaki Sunaga, and Joost N. P. van Stralen. The DIRAC code for relativistic molecular calculations. *The Journal of Chemical Physics*, 152(20):204104, May 2020.
- [113] Guangming Wang, Abdulgani Annaberdiyev, Cody A. Melton, M. Chandler Bennett, Luke Shulenburg, and Lubos Mitas. A new generation of effective core potentials from correlated calculations: 4s and 4p main group elements and first row additions. *The Journal of Chemical Physics*, 151(14):144110, October 2019.
- [114] Abdulgani Annaberdiyev, Guangming Wang, Cody A. Melton, M. Chandler Bennett, Luke Shulenburg, and Lubos Mitas. A new generation of effective core potentials from correlated calculations: 3d transition metal series. *The Journal of Chemical Physics*, 149(13):134108, October 2018.
- [115] B. Meredig, A. Thompson, H. A. Hansen, C. Wolverton, and A. van de Walle. Method for locating low-energy solutions within DFT + U. *Physical Review B*, 82(19):195128, November 2010.
- [116] Jeongnim Kim, Andrew D. Baczewski, Todd D. Beaudet, Anouar Benali, M. Chandler Bennett, Mark A. Berrill, Nick S. Blunt, Edgar Josué Landinez Borda, Michele Casula, David M. Ceperley, Simone Chiesa, Bryan K. Clark, Raymond C. Clay, Kris T. Delaney, Mark Dewing, Kenneth P. Esler, Hongxia Hao, Olle Heinonen, Paul R. C. Kent, Jaron T. Krogel, Ilkka Kylänpää, Ying Wai Li, M. Graham Lopez, Ye Luo, Fionn D. Malone, Richard M. Martin, Amrita Mathuriya, Jeremy McMinis, Cody A. Melton, Lubos Mitas, Miguel A. Morales, Eric Neuscamman, William D. Parker, Sergio D. Pineda Flores, Nichols A. Romero, Brenda M. Rubenstein, Jacqueline A. R. Shea, Hyeondeok Shin, Luke Shulenburg, Andreas F. Tillack, Joshua P. Townsend, Norm M. Tubman, Brett Van Der Goetz, Jordan E. Vincent, D. ChangMo Yang, Yubo Yang, Shuai Zhang, and Luning Zhao. QMCPACK: An open source ab initio quantum Monte Carlo package for the electronic structure of atoms, molecules and solids. *Journal of Physics: Condensed Matter*, 30(19):195901, April 2018.
- [117] P. R. C. Kent, Abdulgani Annaberdiyev, Anouar Benali, M. Chandler Bennett, Edgar Josué Landinez Borda, Peter Doak, Hongxia Hao, Kenneth D. Jordan, Jaron T. Krogel, Ilkka Kylänpää, Joonho Lee, Ye Luo, Fionn D. Malone, Cody A. Melton, Lubos Mitas, Miguel A. Morales, Eric Neuscamman, Fernando A. Reboredo, Brenda Rubenstein, Kayahan Saritas, Shiv Upadhyay, Guangming Wang, Shuai Zhang, and Luning Zhao. QMCPACK: Advances in the development, efficiency, and application of auxiliary

- field and real-space variational and diffusion quantum Monte Carlo. *The Journal of Chemical Physics*, 152(17):174105, May 2020.
- [118] Jaron T. Krogel. Nexus: A modular workflow management system for quantum simulation codes. *Computer Physics Communications*, 198:154–168, January 2016.
- [119] Michele Casula. Beyond the locality approximation in the standard diffusion Monte Carlo method. *Physical Review B*, 74(16):161102, October 2006.
- [120] Luboš Mitáš, Eric L. Shirley, and David M. Ceperley. Nonlocal pseudopotentials and diffusion Monte Carlo. *The Journal of Chemical Physics*, 95(5):3467–3475, September 1991.

Appendix A: Pseudopotentials

1. Optimization Methods

The objective function \mathcal{O}^2 consists of energy gaps $\Delta E_{ECP}^{(s)}$ calculated using CCSD(T) and single-particle orbital eigenvalues $\epsilon_{ECP}^{(i)}$ to be matched with the relativistic AE counterparts:

$$\mathcal{O}^2 = \sum_{s \in S} w_s (\Delta E_{AE}^{(s)} - \Delta E_{ECP}^{(s)})^2 + \sum_{i \in L} w_i (\epsilon_{AE}^{(i)} - \epsilon_{ECP}^{(i)})^2 \quad (\text{A1})$$

where S is the number of considered energy gaps, and L is the highest occupied angular momentum channel.

Throughout the main text, the ECP errors are assessed via the mean absolute deviation (MAD) from a large set of AE atomic gaps, which include states such as electron affinity, first, second, and third ionization potentials, as well as neutral excitations:

$$\text{MAD} = \frac{1}{N} \sum_i^N |\Delta E_i^{\text{ECP}} - \Delta E_i^{\text{AE}}|. \quad (\text{A2})$$

Low-lying gaps such as electron affinity, first ionization potential, and some neutral excitations are also considered:

$$\text{LMAD} = \frac{1}{n} \sum_i^n |\Delta E_i^{\text{ECP}} - \Delta E_i^{\text{AE}}| \quad (\text{A3})$$

where $n < N$. Finally, a weighted MAD (WMAD) is also shown to capture the biases from all states with an appropriate weight:

$$\text{WMAD} = \frac{1}{N} \sum_i^N \frac{100\%}{\sqrt{|\Delta E_i^{\text{AE}}|}} |\Delta E_i^{\text{ECP}} - \Delta E_i^{\text{AE}}|. \quad (\text{A4})$$

The UCCSD(T) calculations were carried out using the MOLPRO package [111]. For COSCI calculations, we used the DIRAC code [112].

2. Sn ccECP

a. Sn: Atomic Spectrum Errors

Table 4 shows the Sn atomic spectrum errors of various core approximations. This data is summarized in the main text, Figure 2.

In Table 5, the full-relativistic ECP errors are shown for ccECP and MDFSTU. These calculations include explicit spin-orbit interactions.

b. Sn: Initial Guess and Optimization

The exponents of Sn ccECP were adopted from SDFSTU and kept frozen during optimizations. A regularizing local channel was added to SDFSTU, and optimizations started from this ECP. Note that SDFSTU was optimized to match the energies of various single-particle states $n\ell$ with varying numbers of n and ℓ .

ccECP optimization included orbital eigenvalues and atomic gaps shown in Table 4. The UCCSD(T) atomic spectrum overfitting showed underbinding tendency, while eigenvalue overfitting showed overbinding tendency. A good balance between spectrum and eigenvalues was found. The total energy was given a very small weight.

c. Sn: ccECP Parameters

Listing 1 provides the final form of Sn ccECP as AREP and SO terms.

Listing 1: Sn ccECP parameters in Molpro ECP format.

ECP, Sn, 46, 3, 2		
4 !ul		
1,	2.000000,	4.000000
3,	2.000000,	8.000000
2,	2.000000,	-12.706546
2,	1.000000,	-0.237233
2 !s		
2,	2.000000,	48.172258
2,	1.000000,	-4.559077
2 !p		
2,	2.000000,	48.856272
2,	1.000000,	-1.913865
2 !d		
2,	0.666000,	6.850466
2,	0.333000,	-0.247154
2 !p-so		
2,	2.716017,	-2.371998
2,	1.359517,	2.093748
2 !d-so		
2,	0.300000,	-0.857741
2,	0.520563,	3.223343

d. Sn: Kinetic Energy Cutoff

Table 6 shows the Sn ccECP energy convergence with respect to plane wave cutoff E_C . Note that $E_C = 100$ Ry is enough for converged calculations.

e. Sn: correlation consistent basis set optimization

Gaussian-type, correlation-consistent basis sets suitable for molecular calculations using quantum chem-

TABLE 4: Sn atom scalar relativistic (DKH) AE gaps and relative errors for various core approximations. The core is taken as core=[Kr]4d¹⁰ (46 core, 4 valence electrons). UCCSD(T) method with uncontracted aug-cc-pwCVQZ basis set was used. MAD stands for mean absolute deviation, LMAD is MAD for low-lying states (EA, IP1, IP2), and WMAD is a weighted MAD where the weights are 100%/√|Δ^{AE}|. “Q.” represents the charge of the state. All values are in eV.

State	Q.	AE	LANL2	UC	MDFSTU	MWBSTU	BFD	SDFSTU	TN-DF	CRENBS	SBKJC	ccECP
[core]5s ² 5p ²	0	0.000										
[core]5s ² 5p ³	-1	-1.406	0.007	-0.005	-0.020	-0.013	-0.028	-0.023	-0.018	-0.015	-0.021	-0.021
[core]5s ² 5p ¹	+1	7.317	-0.106	-0.093	-0.058	-0.076	-0.053	-0.031	-0.044	-0.046	-0.035	-0.004
[core]5s ² 6s ¹	+1	13.998	-0.236	-0.196	-0.089	-0.111	-0.087	-0.036	-0.114	-0.098	-0.070	0.031
[core]5s ² 5d ¹	+1	14.577	-1.034	-0.838	-0.882	-0.810	-0.844	-0.910	-0.771	-0.780	-0.779	-0.762
[core]5s ²	+2	21.569	-0.311	-0.307	-0.223	-0.273	-0.227	-0.137	-0.173	-0.162	-0.136	-0.042
[core]5s ¹ 5d ¹	+2	39.156	-1.291	-1.122	-1.092	-1.048	-0.991	-1.056	-0.776	-0.741	-0.743	-0.491
[core]5s ¹	+3	52.080	-1.407	-1.334	-1.210	-1.208	-1.220	-1.085	-0.964	-0.945	-0.915	-0.798
MAD			0.627	0.557	0.510	0.506	0.493	0.468	0.409	0.398	0.386	0.307
LMAD			0.141	0.135	0.100	0.121	0.103	0.064	0.079	0.074	0.064	0.022
WMAD[%]			12.099	10.584	9.756	9.638	9.480	8.967	7.986	7.781	7.551	6.074

TABLE 5: Sn atomic excitation errors for ccECP versus MDFSTU in SOREP forms. The errors are shown for full-relativistic X2C AE gaps using COSCI. All values are in eV.

Configuration	Term	AE	ccECP	MDFSTU
5s ² 5p ²	³ P ₀	0.0000	0.0000	0.0000
	³ P ₁	0.1862	0.0065	0.0187
	³ P ₂	0.4236	0.0083	0.0324
	¹ D ₂	1.3200	-0.0229	0.0114
	¹ S ₀	2.7526	-0.0758	-0.0269
5s ² 5p ³	⁴ S _{3/2}	0.0000	0.0000	0.0000
	² D _{3/2}	1.1016	-0.0348	-0.0278
	² D _{5/2}	1.1654	-0.0314	-0.0192
	² P _{1/2}	1.9002	-0.0520	-0.0343
	² P _{3/2}	2.0274	-0.0473	-0.0192
5s ² 5p ¹	² P _{1/2}	0.0000	0.0000	0.0000
	² P _{3/2}	0.5218	0.0062	0.0378
5s ² 5d ¹	² D _{3/2}	0.0000	0.0000	0.0000
	² D _{5/2}	0.0234	0.0000	0.0037
MAD			0.0285	0.0232

TABLE 6: QUANTUM ESPRESSO SCF kinetic energy cutoff convergence for Sn ccECP. [10 × 10 × 10] Angstrom cell and PBE functional was used. 100 Ry is enough to achieve 1 meV/e convergence.

E _C [Ry]	Total Energy [Ry]
50	-6.74263240
100	-6.74298953
150	-6.74300760
200	-6.74301096

istry packages were optimized using HF and CCSD(T) methods. The *s* and *p* contraction exponents and co-

efficients were obtained from HF, while the correlation-consistent terms were optimized by CCSD(T) using an even-tempered scheme. For details of this optimization methodology, see Ref. [113]. (aug)-cc-pVnZ basis sets and ECPs given in MOLPRO, NWCHEM, GAMESS, GAUSSIAN, and DIRAC code formats as well as UPF files for QUANTUM ESPRESSO and XML files for QMCPACK can be found in Ref. [46].

3. Tb ccECP

a. Tb: Orbital Eigenvalues

AE and ccECP single-particle eigenvalues for low-lying [Xe]4f⁹6s² and [Xe]4f⁸5d¹6s² states are listed in Tables 7 and 8 respectively. In both cases, the eigenvalues of 4s, 4p, and 4d orbitals are significantly lower than the valence eigenvalues, indicating the validity of the chosen core↔valence partitioning. Also, note that the eigenvalue of 4f seems to be too small to be considered a core state.

b. Tb: Atomic Spectrum Errors

Table 9 shows the scalar-relativistic Tb atomic spectrum errors for various core approximations. Note that ccECP is accurate up to *Q* = +3. As the nominal charge of Tb in the solid is *Q* = +3, this indicates that the obtained ccECP should be accurately transferable to the solid.

Table 10 shows the full-relativistic Tb J-splitting errors for ccECP. An excellent agreement is obtained within 0.01 eV of the AE data.

TABLE 7: Tb scalar relativistic (DKH) AE and ccECP eigenvalues [Ha] of $[\text{Xe}]4f^96s^2$ state. RHF method in D_{2h} point group with uncontracted aug-cc-pwCVTZ basis set was used. Eigenvalues for s , p_x , d_{yz} , and f_{xyz} are shown.

Orbital	AE	ccECP
1s	-1920.3973	
2s	-322.8168	
2p	-287.0796	
3s	-73.4819	
3p	-62.2062	
3d	-47.2270	
4s	-15.4251	
4p	-11.6218	
4d	-6.1995	
5s	-2.1357	-2.1438
5p	-1.1464	-1.1581
4f	-0.4358	-0.3897
6s	-0.1850	-0.1848

TABLE 8: Tb scalar relativistic (DKH) AE and ccECP eigenvalues [Ha] of $[\text{Xe}]4f^85d^16s^2$ state. RHF method in D_{2h} point group with uncontracted aug-cc-pwCVTZ basis set was used. Eigenvalues for s , p_x , d_{xy} , and f_{xyz} are shown.

Orbital	AE	ccECP
1s	-1920.6455	
2s	-323.0878	
2p	-287.3516	
3s	-73.7872	
3p	-62.5295	
3d	-47.5373	
4s	-15.7199	
4p	-11.9329	
4d	-6.4678	
5s	-2.2948	-2.2946
5p	-1.2872	-1.2882
4f	-0.8547	-0.8501
5d	-0.2468	-0.2589
6s	-0.1998	-0.1984

c. Tb: Initial Guess and Optimization

The following steps were taken to generate a reasonable initial guess for CCSD(T) atomic spectrum optimizations. The idea is to initially separate the optimization into steps that only depend on one non-local channel part of the ECP. In the following steps, all AE calculations use DKH scalar relativity with an uncontracted aug-cc-pwCVTZ basis set.

1. Calculate AE HF state for the “core-configuration” core= $[\text{Kr}]4d^{10}$.
2. Calculate AE HF state for an “s-only” state. In this

TABLE 9: Tb scalar relativistic (DKH) AE gaps and relative errors for various core approximations. The core is taken as $[\text{Kr}]4d^{10}$ (46 core, 19 valence electrons). UCCSD(T) method with uncontracted aug-cc-pwCVTZ basis set was used. MAD stands for mean absolute deviation, LMAD is MAD for 6 low-lying states, and WMAD is a weighted MAD where the weights are $100\%/\sqrt{|\Delta^{AE}|}$. All values are in eV. “Q.” represents the charge of the state. Opium is an ECP generated using the OPIUM code with a scalar-relativistic PBE and Troullier-Martins scheme.

State	Q.	AE	Opium	SBKJC	ccECP	UC
$[\text{Xe}]4f^86s^25d^1$	0	0.000				
$[\text{Xe}]4f^96s^2$	0	0.577	2.633	-1.306	-0.031	0.071
$[\text{Xe}]4f^86s^15d^2$	0	1.337	-0.239	-0.232	-0.050	-0.045
$[\text{Xe}]4f^86s^26p^1$	0	1.776	0.299	-0.511	-0.027	0.039
$[\text{Xe}]4f^96s^1$	+1	6.420	2.766	-1.324	-0.052	0.059
$[\text{Xe}]4f^86s^15d^1$	+1	6.204	-0.020	-0.342	-0.037	-0.018
$[\text{Xe}]4f^86s^2$	+1	6.352	0.372	-0.532	-0.029	0.045
$[\text{Xe}]4f^9$	+2	17.961	3.084	-1.252	-0.033	0.029
$[\text{Xe}]4f^85d^1$	+2	18.482	0.116	-0.228	-0.027	-0.058
$[\text{Xe}]4f^86s^1$	+2	19.316	0.452	-0.534	-0.072	0.024
$[\text{Xe}]4f^8$	+3	38.934	0.723	-0.386	-0.064	-0.021
$[\text{Xe}]4f^75d^1$	+3	44.715	-3.116	1.281	0.753	-0.110
$[\text{Xe}]4f^76s^1$	+3	48.582	-2.856	0.759	0.559	-0.019
$[\text{Xe}]4f^7$	+4	77.358	-2.512	1.049	0.583	-0.083
$[\text{Kr}]4d^{10}5s^25p^34f^7$	+7	342.117	-2.841	-1.209	-1.262	-0.502
MAD			1.573	0.782	0.256	0.080
LMAD			1.130	0.699	0.038	0.039
WMAD[%]			53.098	29.947	3.709	2.112

case, we used $[\text{core}]5s^26s^2$. The AE valence energy is obtained by subtracting out the core energy from the 1^{st} step. Now optimize the s -part of the ECP by matching the total valence energy and orbital eigenvalues of $5s^2$ and $6s^2$. All other ECP channel coefficients are set to zero (including the local).

3. Similar to step 2, now obtain AE valence energy for a “ p -only” state. We used $[\text{core}]5p^6$ in this case. Again, match the total valence energy and $5p^6$ orbital eigenvalue by optimizing the p -part of the ECP.
4. Do similar steps for the d -part of the ECP. We used $[\text{core}]5d^5$ as the reference here.
5. The final non-local channel used is the f -part. Similar steps are repeated for this part using $[\text{core}]4f^7$ reference state.
6. All the optimized parameters from steps 2-5 are combined into one ECP. Now we have added a local channel which has been set to zero so far. Again the local channel is optimized for the total valence energy and orbital eigenvalues of an AE reference state. The reference state was chosen as the trivalent state of $[\text{core}]5s^25p^64f^86s^25d^1$.

In optimization steps 2-5, two Gaussians were used for each step where both exponents and coefficients are op-

TABLE 10: Tb experimental (Expt.) and all-electron (AE) atomic J-splitting gaps due to spin-orbit coupling. ccECP represents the COSCI method errors for SOREP ccECP when compared to full-relativistic X2C AE data. All values are in eV.

Configuration	Term	Expt.	AE	ccECP
[Xe]4f ⁹ 6s ²	⁶ H _{15/2} ^o	0.0000	0.0000	0.0000
	⁶ H _{13/2} ^o	0.3436	0.3588	-0.0022
	⁶ H _{11/2} ^o	0.5791	0.6150	-0.0079
	⁶ H _{9/2} ^o	0.7656	0.8121	-0.0130
[Xe]4f ⁸ 5d ¹ 6s ²	⁸ G _{13/2}	0.0000	0.0000	0.0000
	⁸ G _{15/2}	0.0219	0.0075	0.0010
	⁸ G _{11/2}	0.0278	0.0580	0.0021
	⁸ G _{9/2}	0.1346	0.1716	0.0040
	⁸ G _{7/2}	0.2646	0.2863	0.0025
	⁸ G _{5/2}	0.3582	0.3751	-0.0006
	⁸ G _{3/2}	0.4241	0.4399	-0.0032
	⁸ G _{1/2}	0.4628	0.4792	-0.0050
[Xe]4f ⁹ 6s ¹	($\frac{15}{2}, \frac{1}{2}$) ₈ ^o	0.0000	0.0000	0.0000
	($\frac{15}{2}, \frac{1}{2}$) ₇ ^o	0.1260	0.1656	-0.0391
	($\frac{13}{2}, \frac{1}{2}$) ₇ ^o	0.3732	0.4019	-0.0301
	($\frac{13}{2}, \frac{1}{2}$) ₆ ^o	0.4392	0.4783	-0.0224
[Xe]4f ⁹	⁶ H _{15/2} ^o	0.0000	0.0000	0.0000
	⁶ H _{13/2} ^o	0.3477	0.3593	-0.0014
	⁶ H _{11/2} ^o	0.5870	0.6160	-0.0068
	⁶ H _{9/2} ^o	0.7759	0.8137	-0.0115
	⁶ H _{7/2} ^o	0.9202	0.9660	-0.0153
	⁶ H _{5/2} ^o	1.0273	1.0792	-0.0182
[Xe]4f ⁸ 5d ¹	⁸ G _{13/2}	0.0000	0.0000	0.0000
	⁸ G _{11/2}	0.0305	0.0546	0.0027
	⁸ G _{15/2}	0.0376	0.0214	0.0018
	⁸ G _{9/2}	0.1361	0.1626	0.0045
	⁸ G _{7/2}	0.2509	0.2691	0.0025
	⁸ G _{5/2}	0.3356	0.3526	-0.0008
	⁸ G _{3/2}	0.3959	0.4136	-0.0035
	⁸ G _{1/2}	0.4317	0.4507	-0.0053
[Xe]4f ⁸ 6p ¹	($6, \frac{1}{2}$) _{11/2} ^o	0.0000	0.0000	0.0000
	($6, \frac{1}{2}$) _{13/2} ^o	0.0265	0.0045	0.0021
	($5, \frac{1}{2}$) _{9/2} ^o	0.2222	0.2260	0.0110
	($5, \frac{1}{2}$) _{11/2} ^o	0.3215	0.3192	-0.0147
	($4, \frac{1}{2}$) _{7/2} ^o	0.3628	0.3792	0.0101
	($4, \frac{1}{2}$) _{9/2} ^o	0.4827	0.4918	-0.0005
MAD				0.0082

timized. In step 6 (local channel), two Gaussians and two additional Gaussian terms multiplied with $1/r$ and r were used, similar to BFD or ccECP parametrizations.

All exponents were constrained from below at 1.5 to prevent the generation of long, un-physical potential tails, and they were also constrained from above at 9.0 to prevent very high kinetic energy cut-offs in plane-wave codes. For f and local channels, the exponents were constrained from above at 5.0 since it was observed that

these channels are the main factors in deciding the plane-wave cut-offs. The same constraints are also applied in the rest of the optimizations as well. To overcome getting trapped in the parameter space, a few starting parameters were tried until small error residuals were obtained.

This concludes the generation of an initial guess to be optimized in CCSD(T) atomic gap optimizations. The rest of the optimization includes atomic spectrum gaps using CCSD(T), eigenvalues of neutral and charge= +3 trivalent states, and the norm for a chosen neutral state.

d. Tb: ccECP Parameters

Listing 2 provides the final form of Tb ccECP as AREP and SO terms.

Listing 2: Tb ccECP parameters in Molpro ECP format.

```

ECP, Tb, 46, 4, 3
4 !ul
1, 4.526254, 19.000000
3, 3.879308, 85.998831
2, 4.406058, -85.722649
2, 1.899664, -3.133952
2 !s
2, 8.996757, 161.119164
2, 5.104371, 89.334835
2 !p
2, 7.640657, 88.693021
2, 3.878305, 57.109488
2 !d
2, 7.456305, 55.901690
2, 2.530445, 29.364333
2 !f
2, 4.939345, -23.952530
2, 3.912490, -7.090915
1 !p-so
4, 2.080465, 2.963688
1 !d-so
4, 2.660751, 0.922456
1 !f-so
4, 4.708055, 0.178089

```

e. Tb: Kinetic Energy Cutoff

Table 11 shows the Tb ccECP energy convergence with respect to plane wave cutoff E_C . Note that $E_C = 600$ Ry is enough for converged calculations.

f. Tb: correlation consistent basis set optimization

For the optimization of Gaussian-type, correlation-consistent basis sets for molecular calculations using quantum chemistry methods, we follow a methodology

TABLE 11: QUANTUM ESPRESSO SCF kinetic energy cutoff convergence for Tb ccECP. $[10 \times 10 \times 10]$ Angstrom cell is used with PBE functional. 600 Ry is enough to achieve 1 meV/ e convergence.

E_C [Ry]	Total Energy [Ry]
300	-258.21011528
400	-258.82039730
500	-258.87654695
600	-258.88182883
700	-258.88237251
800	-258.88243440

similar to what is described in the Supplemental of Ref. [114]. Briefly, the contraction exponents were first optimized via HF for the trivalent state $[\text{Xe}]4f^85d^16s^2$ of Tb. Next, we use a CI calculation of this trivalent state to obtain the atomic natural orbitals and use these as contractions for s , p , d , and f channels. By freezing excitations from the $5s$ and $5p$ orbitals, we optimize valence-only correlation-consistent and polarization terms using CI to form cc-pVnZ basis sets. Then, an extra ‘‘core’’ term is added to each channel by optimizing the full space in CI to form the cc-pCVnZ basis sets. For the final form of these basis sets, see Ref. [46] where they can be found in MOLPRO, NWCHEM, GAMESS, GAUSSIAN, and DIRAC code formats as well as UPF format for QUANTUM ESPRESSO and XML format for QMCPACK.

Appendix B: DFT+ U Methods and Data

All DFT+ U calculations were carried with QUANTUM ESPRESSO package [69–71]. DFT+ U is well-known to converge to meta-stable states depending on the given initial guess for the Hubbard occupation matrix. To overcome this issue, we use a method similar to ramping method described in Ref. [115]. Specifically, first, we converge a DFT+ U calculation with a very small U value, such as 10^{-16} eV. Then, the converged charge density, orbitals, and Hubbard occupation matrices are directly provided as an initial guess for the desired value of U , essentially skipping the adiabatic ramping of U . On a few occasions, we tested that this method indeed results in lower energies than the default values for Hubbard occupations.

Tables 12, 13, 14 provide the data for convergence of gaussian spreading, kinetic energy cutoff, and k -mesh DFT parameters, respectively. Fully-converged bulk calculation parameters used in the study are 0.001 Ry gaussian spreading, 600 Ry kinetic energy cutoff, and $[8 \times 8 \times 8]$ k -mesh in the bulk primitive cell. Slab calculations used $[8 \times 8 \times 1]$ k -mesh in the SCF calculations, which were observed to be converged with respect to k -mesh. Hybrid DFA calculations employed a smaller $[4 \times 4 \times 4]$ k -mesh due to the high cost of hybrids in bulk systems.

To facilitate the SCF convergence in the large k -mesh

TABLE 12: Convergence of QUANTUM ESPRESSO gaussian spreading (Ry) for Brillouin-zone integration in bulk TbMn_6Sn_6 . k -mesh = $[2 \times 2 \times 1]$. PBE functional. 600 Ry kinetic energy cutoff. Unconstrained total spin magnetization. 0.001 Ry gaussian spreading was chosen to be used throughout the study.

Spreading [Ry]	Total Energy [Ry]	M^s [μ_B]
0.0080	-1549.08702247	10.39
0.0040	-1549.07374172	8.97
0.0020	-1549.07044686	9.02
0.0010	-1549.06951107	9.08
0.0005	-1549.06922402	9.02
0.0001	-1549.06902797	9.00

TABLE 13: Convergence of QUANTUM ESPRESSO SCF kinetic energy cutoff in bulk TbMn_6Sn_6 . k -mesh = $[2 \times 2 \times 1]$. PBE functional. Unconstrained total spin magnetization. 600 Ry was chosen to be used throughout the study.

E_C [Ry]	Total Energy [Ry]	M^s [μ_B]
400	-1549.00725031	9.09
450	-1549.04997024	9.09
500	-1549.06357348	9.09
550	-1549.06803239	9.08
600	-1549.06951102	9.08
650	-1549.07005881	9.08

calculations, we first converged the calculations in a coarse k -mesh of $[2 \times 2 \times 1]$. We then carried out non-self-consistent calculations (nscf) for a desired dense k -mesh using the charge densities from the previous coarse k -mesh. The resulting orbitals from the nscf and the previously obtained charge density were given as an initial guess to the dense k -mesh SCF, which showed very robust convergence behavior.

Table 15 shows the effect of applying Hubbard U on Mn- $3d$, Tb- $4f$, Tb- $5d$, and Sn- $5p$ orbitals. Note that there are significant changes in magnetic moments and cell magnetizations when U is applied on Mn- $3d$ orbitals. However, the corresponding changes are much smaller when U is applied to other subspaces. This is further explored by plotting the band structure of TbMn_6Sn_6 when a + U is applied on Tb $4f$ orbitals in addition to the Mn $3d$ orbitals. Figure 16 shows this band structure using LDA+ $U_{Mn}^{3d}(-0.5 \text{ eV})+U_{Tb}^{4f}(1.0 \text{ eV})$ DFA. We observe that this band structure is indistinguishable to the human eye from Figure 13a where the + U is not applied on Tb $4f$ orbitals. This indicates that Tb $4f$ orbitals are already sufficiently localized, and the application of + U_{Tb}^{4f} is not crucial for this study, where we focus on small energy scales around E_F .

Figure 17, and Figure 18 demonstrate how the atomic moments and charges, respectively, change as different U_{Mn}^{3d} values are applied on LDA using averaged SOC effects (AREP). Figure 19 shows the Mn atomic moment,

TABLE 14: Convergence of QUANTUM ESPRESSO SCF k -mesh in bulk TbMn₆Sn₆. PBE functional. Unconstrained total spin magnetization (M^s [μ_B]). 600 Ry kinetic energy cutoff. Approximate spin magnetic moments m^s [μ_B] (integrated on an atomic sphere of a certain radius) are shown for each species. m_{Sn}^s values are averaged over 3 slightly different values (of range $\approx 0.01\mu_B$). E_F is the Fermi level. $[8 \times 8 \times 8]$ k -mesh was used throughout the study.

k -mesh	Total Energy [Ry]	m_{Tb}^s	m_{Mn}^s	m_{Sn}^s	M^s	$ M^s $	E_F [eV]
$[2 \times 2 \times 2]$	-1549.05326051	-6.2141	2.7677	-0.1021	9.32	24.70	11.8286
$[4 \times 4 \times 4]$	-1549.05680281	-6.2488	2.6583	-0.1071	8.44	24.20	11.7608
$[6 \times 6 \times 6]$	-1549.05705150	-6.2519	2.6522	-0.1115	8.33	24.22	11.7640
$[8 \times 8 \times 8]$	-1549.05700751	-6.2518	2.6345	-0.1141	8.17	24.13	11.7561
$[10 \times 10 \times 10]$	-1549.05679211	-6.2507	2.6346	-0.1134	8.19	24.12	11.7544
$[12 \times 12 \times 12]$	-1549.05661464	-6.2509	2.6335	-0.1136	8.18	24.12	11.7545

TABLE 15: The effect of applying Hubbard $+U$ on Tb $4f$, $5d$, and Sn $5p$ subspaces. LDA+ U [eV] DFA with unconstrained total spin magnetization (M^s [μ_B]) is used. 600 Ry kinetic energy cutoff. Approximate spin magnetic moments m^s [μ_B] (integrated on an atomic sphere of a certain radius) are shown for each species. m_{Sn}^s values are averaged over 3 slightly different values. E_F is the Fermi level. $[8 \times 8 \times 8]$ k -mesh was used in this table.

U_{Mn}^{3d}	U_{Tb}^{4f}	U_{Tb}^{5d}	U_{Sn}^{5p}	m_{Tb}^s	m_{Mn}^s	m_{Sn}^s	M^s	$ M^s $
0.5	0.0	0.0	0.0	-6.2550	2.9040	-0.1002	10.20	25.54
0.0	0.0	0.0	0.0	-6.2601	2.3954	-0.0924	7.09	22.33
-0.5	0.0	0.0	0.0	-6.2282	2.2498	-0.0761	6.51	21.19
-0.5	1.0	0.0	0.0	-6.2359	2.2515	-0.0761	6.51	21.21
-0.5	-1.0	0.0	0.0	-6.2139	2.2474	-0.0759	6.52	21.16
-0.5	0.0	1.0	0.0	-6.2221	2.2481	-0.0759	6.50	21.18
-0.5	0.0	-1.0	0.0	-6.2312	2.2516	-0.0763	6.52	21.20
-0.5	0.0	0.0	1.0	-6.2285	2.2549	-0.0791	6.50	21.26
-0.5	0.0	0.0	-1.0	-6.2277	2.2458	-0.0732	6.53	21.14

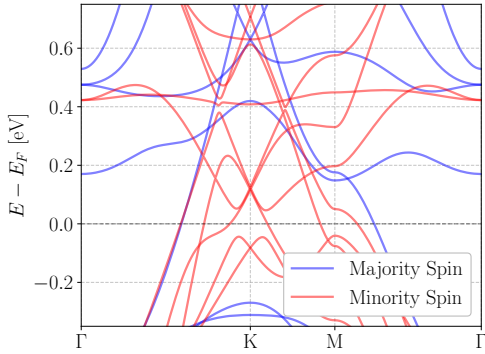


FIG. 16: Bulk band structure of TbMn₆Sn₆ when an additional $+U$ is applied on Tb $4f$ orbitals besides the Mn $3d$ orbitals. Here the DFA is LDA+ U_{Mn}^{3d} (-0.5 eV)+ U_{Tb}^{4f} (1.0 eV). This band structure is indistinguishable from Figure 13a where the $+U_{Tb}^{4f} = 0$.

and cell magnetization as J is included.

Figures 20, 21, and 21 demonstrate the bulk, subsurface, and surface band structures obtained via projections into the atomic Mn- d orbitals. Specifically, these are plotted using the k -resolved, partial density of states

($pDOS$) averaged over different Mn sites:

$$pDOS^{<Mn>} = \sum_i^N pDOS_i^{Mn}(k, E)/N \quad (B1)$$

where $N = 6$ is the number of Mn sites.

In Figure 24, the Fermi surfaces of bulk TbMn₆Sn₆ using scalar-relativistic LDA+ U_{Mn}^{3d} (-0.5 eV) is shown. To obtain the Fermi surface, an SCF calculation with a $[8 \times 8 \times 8]$ k -mesh and a non-SCF calculation with a larger $[20 \times 20 \times 20]$ k -mesh was used. The Fermi surfaces are shown for the majority and minority spin channels.

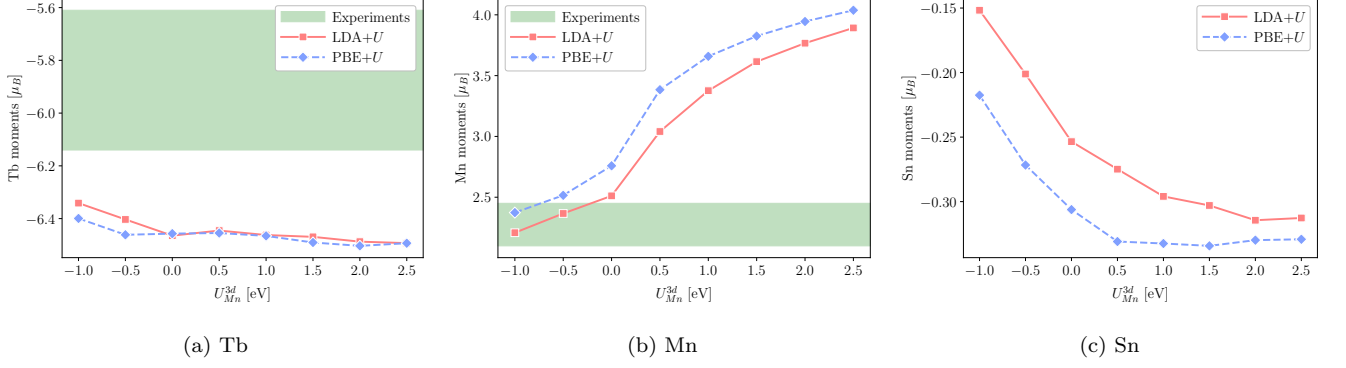


FIG. 17: LDA+ U_{Mn}^{3d} Lowdin atomic moments of (a) Tb, (b) Mn, and (c) Sn as the U_{Mn}^{3d} is varied. Sn values are the averages of three different Sn sites. AREP pseudopotentials are used in these plots.

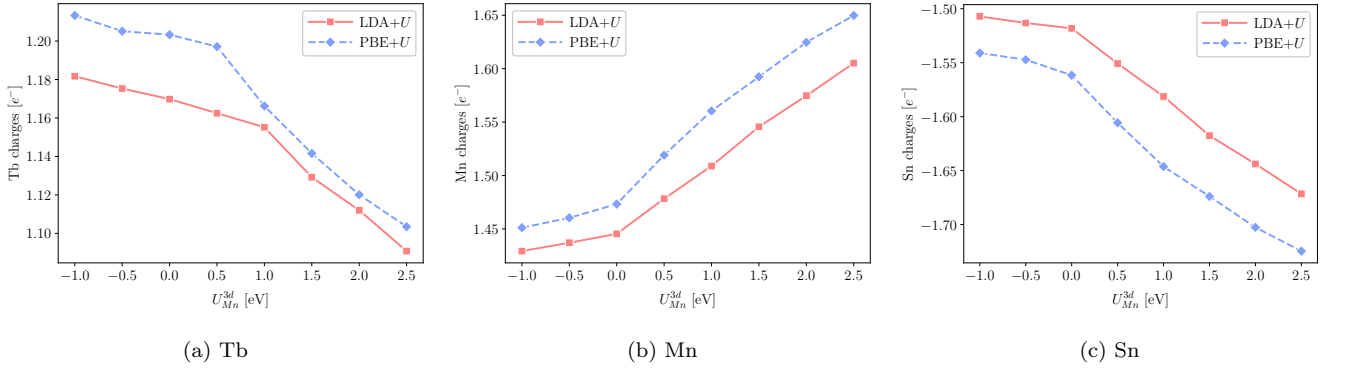


FIG. 18: LDA+ U_{Mn}^{3d} Lowdin atomic effective charges of (a) Tb, (b) Mn, and (c) Sn as the U_{Mn}^{3d} is varied. Sn values are the averages of three different Sn sites. AREP pseudopotentials are used in these plots.

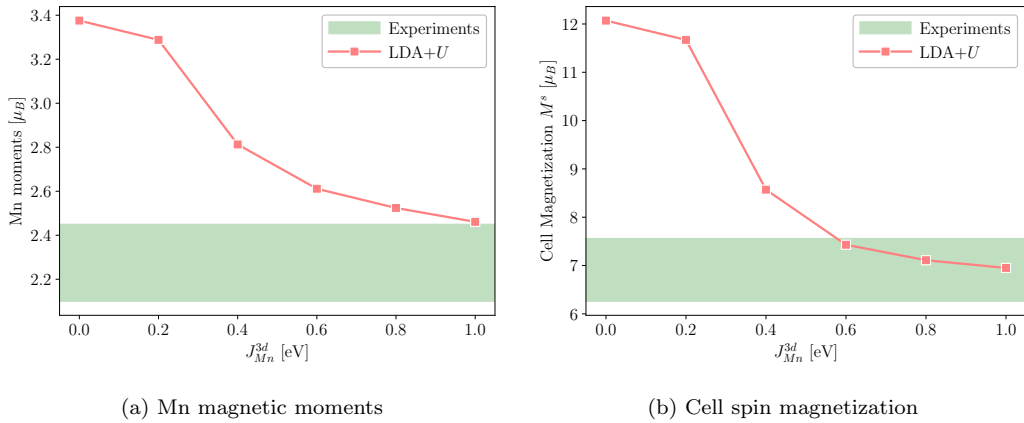


FIG. 19: Comparison of DFT+ $U + J$ and experimental magnetizations. In these plots, $U_{Mn}^{3d} = 1$ eV is fixed, while the J_{Mn}^{3d} is varied. (a) Mn atomic magnetic moments, (b) cell spin magnetization per formula unit. The green-shaded regions represent the envelope of various experimental measurements [1, 6, 7, 17, 19, 22, 23]. In (b), the experimental cell magnetization was added with the Tb orbital magnetization of $M_{Tb}^{orb} = 2.96 \mu_B$ [2] for a proper comparison, $M^s = M_{exp}^{total} + M_{Tb}^{orb}$.

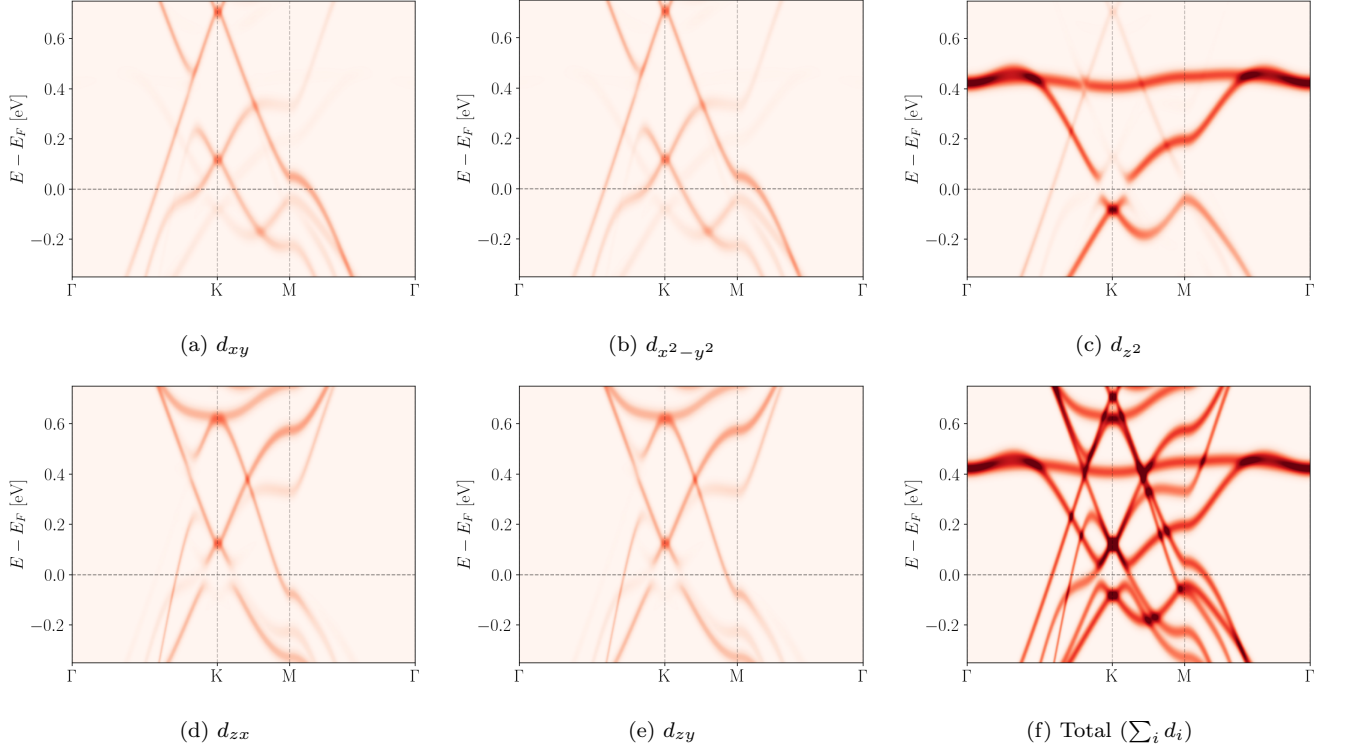


FIG. 20: Minority spin bulk band structures using projections on the atomic Mn d orbitals. The plots show the averages over different Mn atoms.

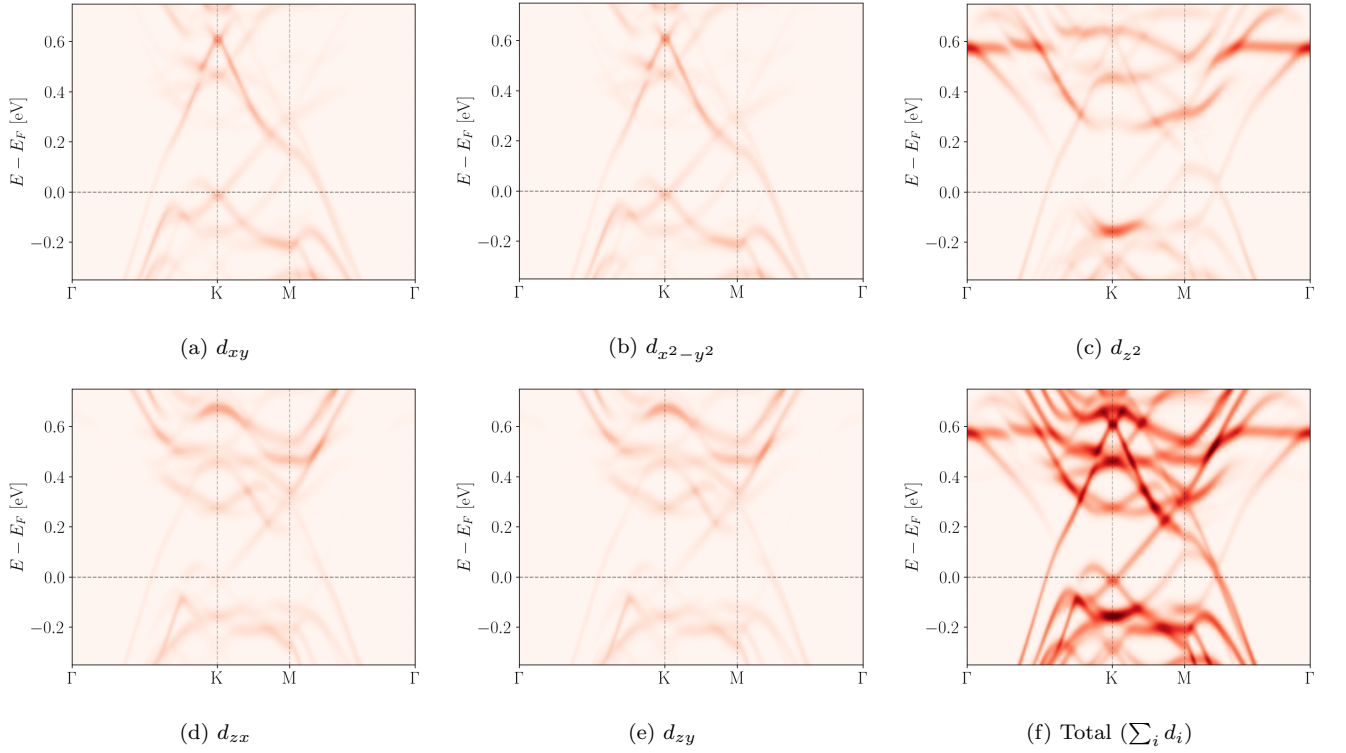


FIG. 21: Minority spin slab band structures using projections on the *subsurface* atomic Mn d orbitals. The plots show the averages over different subsurface Mn atoms.

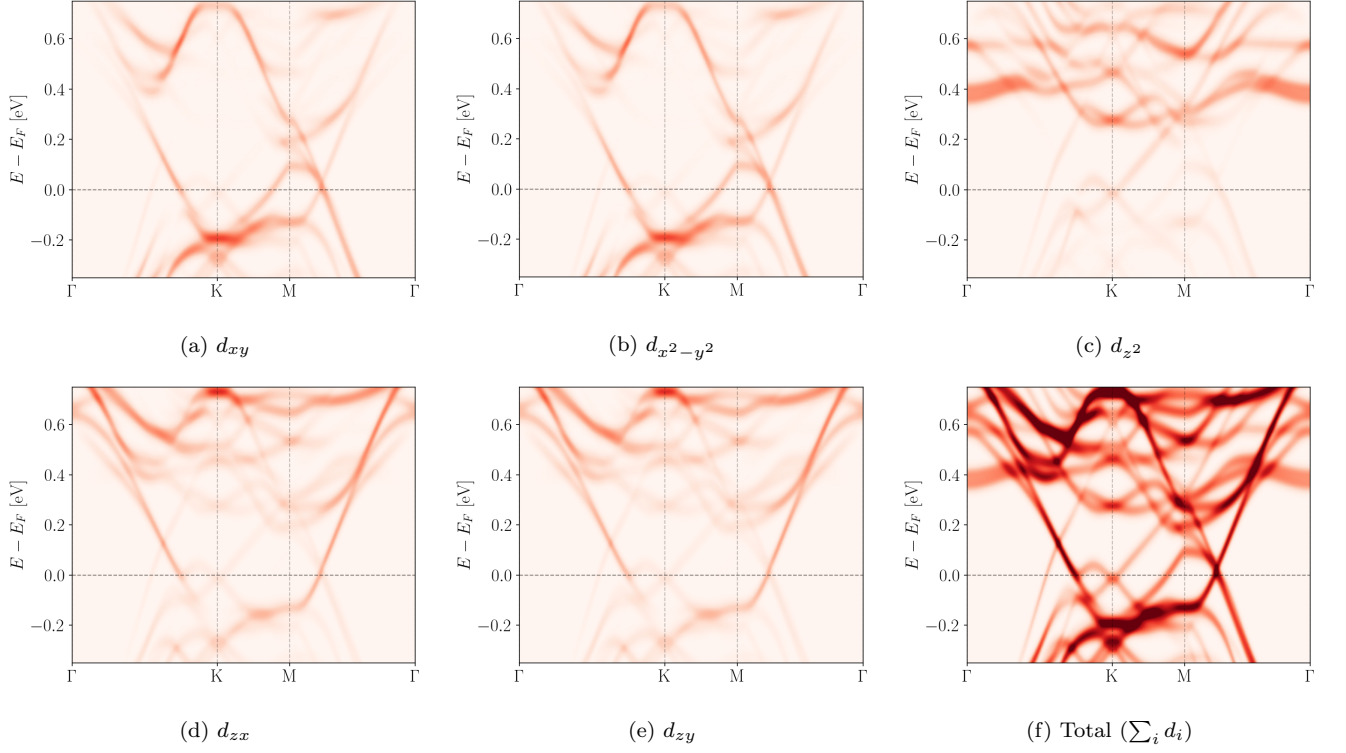


FIG. 22: Minority spin slab band structures using projections on the *surface* atomic Mn d orbitals. The plots show the averages over different surface Mn atoms.

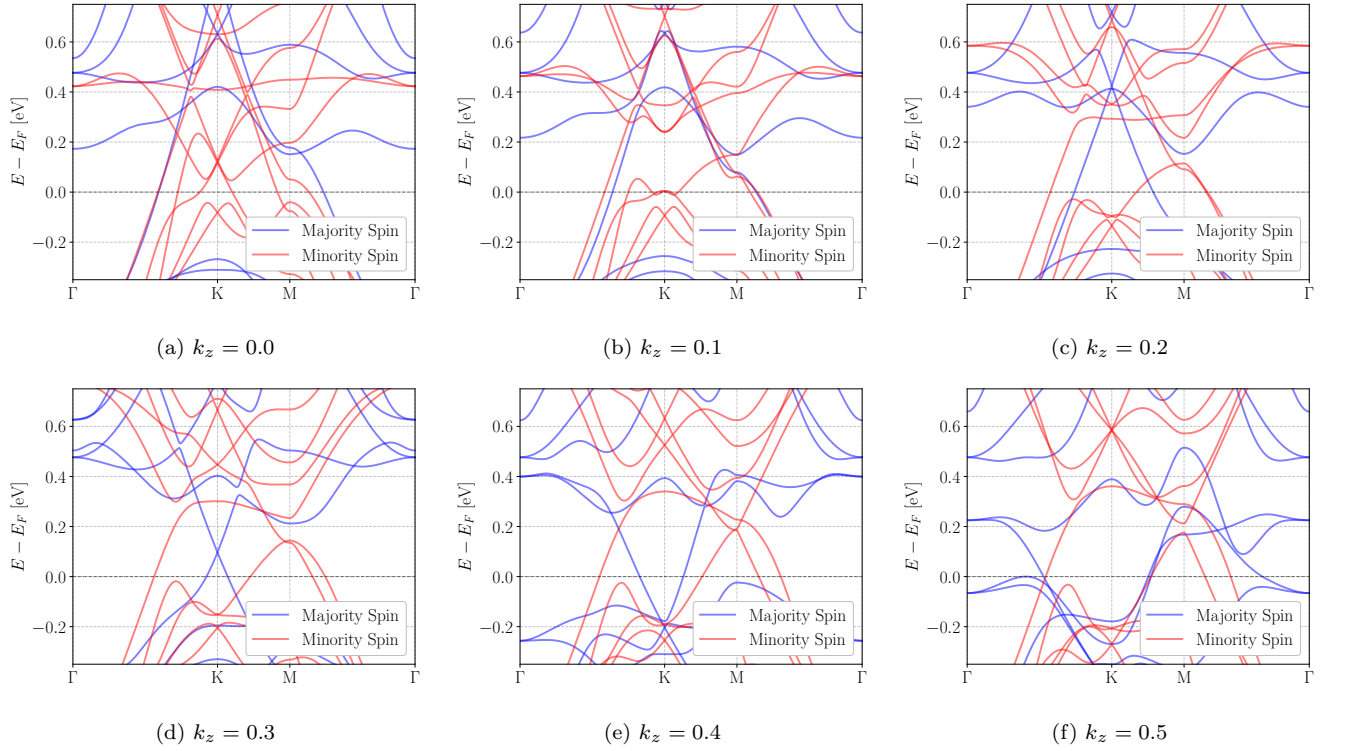
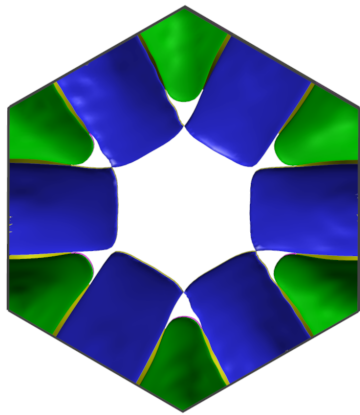
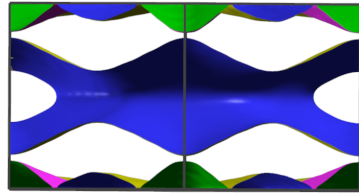


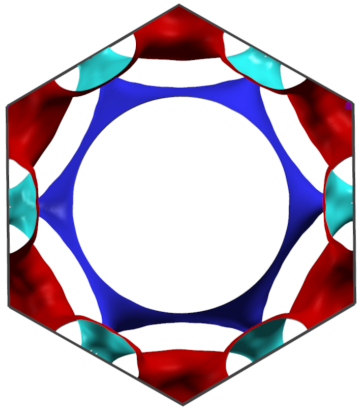
FIG. 23: Bulk band structures of TbMn_6Sn_6 for various k_z values in reciprocal lattice units. The $k_z = 0$ labels Γ , K, M are repeated for $k_z \neq 0$ values for ease of comparison. Note the heavy k_z dispersion of the bands.



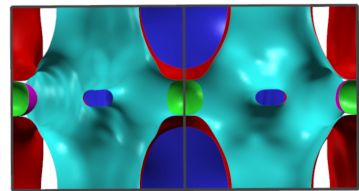
(a) Majority Spin (top view)



(b) Majority Spin (side view)



(c) Minority Spin (top view)



(d) Minority Spin (side view)

FIG. 24: Fermi surfaces of TbMn_6Sn_6 bulk using $\text{LDA}+U_{Mn}^{3d}(-0.5 \text{ eV})$. (a, b) Majority Spin, (c, d) Minority Spin.

Appendix C: QMC Methods and Data

All QMC calculations were carried out using the QMCPACK package [116, 117]. Most calculations were driven by the NEXUS automation tool [118].

All bulk QMC calculations use canonical twist-averaging (CTA) to sample the kinetic energy. In this approach, every twist is charge neutral. In addition, every twist is enforced to have the same cell magnetization:

$$M^s(\text{twist}) = N_e^{\text{up}} - N_e^{\text{down}} = \text{Const.} \quad (\text{C1})$$

namely, every twist has the same magnetization as the twist-averaged magnetization of the cell. At each twist, the orbitals are occupied using the lowest Kohn-Sham eigenvalues in each spin channel.

All molecular and bulk Jastrow functions were optimized using energy minimization in VMC. For bulk calculations, the Jastrow was optimized using $k = \Gamma$ twist and reused for other twists. This optimization was carried out for LDA orbitals at $M^s = 7 \mu_B$ and reused for all other DFAs and M^s values. Fixing the Jastrow part of the trial wave function was done to achieve improved energy differences due to the determinantal part of the trial wave function.

Figure 25 shows the DMC timestep extrapolation for Tb^{3+} cation. The extrapolated energy is within the error bars of $\tau = 0.001 \text{ Ha}^{-1}$; therefore, this timestep was used for all molecular systems for comparison with CCSD(T) method. For bulk QMC calculations where we don't compare with CCSD(T), we use a larger $\tau = 0.02 \text{ Ha}^{-1}$ timestep.

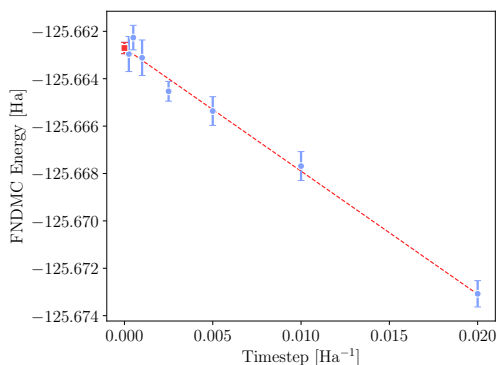


FIG. 25: DMC timestep extrapolation for Tb^{3+} cation.

Table 16 shows how the total energy converges as the number of integration points for non-local ECP evaluation is increased. We find that a larger number of integration points is required for Tb compared to Mn. For sufficiently dense sampling, we see that the VMC energy agrees with ROHF energy. All DMC calculations use the

T-moves algorithm [119] in sampling the non-local part of the ECPs.

Orbitals in QMC calculations were represented by a B-spline mesh. The quality of the mesh was tested by comparing the total energies [Ha] and variances [Ha²] using VMC with ROHF Slater-determinant trial wave function (no Jastrows). N(quad) is the number of integration points for non-local ECP evaluation in VMC. Exact (ROHF/cc-pVTZ) energy is also shown for comparison. Note that a higher N(quad) is needed for Tb (N(quad)=26) when compared to Mn (N(quad)=12).

N(quad)	Tb(var)	Tb(en)	Mn(var)	Mn(en)
12	374.4(5)	-126.279(2)	12.60(5)	-103.2240(2)
18	140.0(2)	-126.280(1)	12.60(5)	-103.2240(2)
26	17.76(2)	-126.2507(4)	12.60(5)	-103.2241(2)
32	17.80(4)	-126.2504(4)	12.60(5)	-103.2241(3)
50	17.76(3)	-126.2502(4)	12.60(5)	-103.2241(2)
ROHF		-126.25074		-103.22389

paring it against a hybrid orbital of localized and B-spline representation, see Table 17. Note that the employed full B-spline representation results in the same energy as the hybrid representation, showing that the spline mesh is sufficiently dense.

In Figure 26, we show the VMC energy extrapolations with respect to energy variance for molecular systems considered in this work. In most cases, the extrapolated VMC energy is below the DMC/SJ₁₂₃ and above the nearly-exact UCCSD(T)/CBS. The notable exception is the Sn atom, where the extrapolated energy is slightly below the exact energy since the fixed-node biases are very small.

Table 18 provides the total energies of TbMn_6Sn_6 relevant systems using various methods. Single-reference biases present in QMC calculations were estimated using these total energies.

Appendix D: Bulk and Slab Geometries

Throughout this work, we use the experimental geometry from a neutron diffraction study [23]. The structure is reproduced here in Table 19. In addition, the structure is also provided in XSF format in Table 20.

The slab calculation geometries were adapted from the bulk experimental geometry by appropriately terminating it with an Mn surface. We explored the geometry relaxation of the Mn layer as a function of its distance z to the slab and found no energy gains when z was incremented by 0.01 Angstroms until $\Delta z = 0.45$ Angstroms. See Figure 14 for the geometry of the employed slab. The slab structure is also provided in XSF format in Table 21.

TABLE 17: Probe of QMCPACK orbital representation quality in bulk TbMn_6Sn_6 . Orbitals can be represented with either full B-spline mesh or a hybrid combination of localized atomic basis set around atomic cores and B-splines. The hybrid representation allows for the use of coarser B-spline mesh. The below table shows whether hybrid representation is used or not for each atomic species. Due to memory constraints, a maximum value of 0.9 could be used for the mesh factor. Maximum spherical harmonics (l_{max}) used for each species are Tb: 6, Mn: 5 with a cutoff radius of 1.5 Bohr.

Mesh Factor	Tb-hybrid	Mn-hybrid	Sn-hybrid	Total Energy [Ha]	Kinetic Energy [Ha]	Variance [Ha ²]
0.9	No	No	No	-1540.013(1)	1000.52(2)	33.54(8)
0.7	Yes	Yes	No	-1540.015(1)	1000.56(3)	29.93(2)
0.8	Yes	Yes	No	-1540.016(1)	1000.66(3)	29.99(9)
0.9	Yes	Yes	No	-1540.012(1)	1000.59(3)	29.95(5)

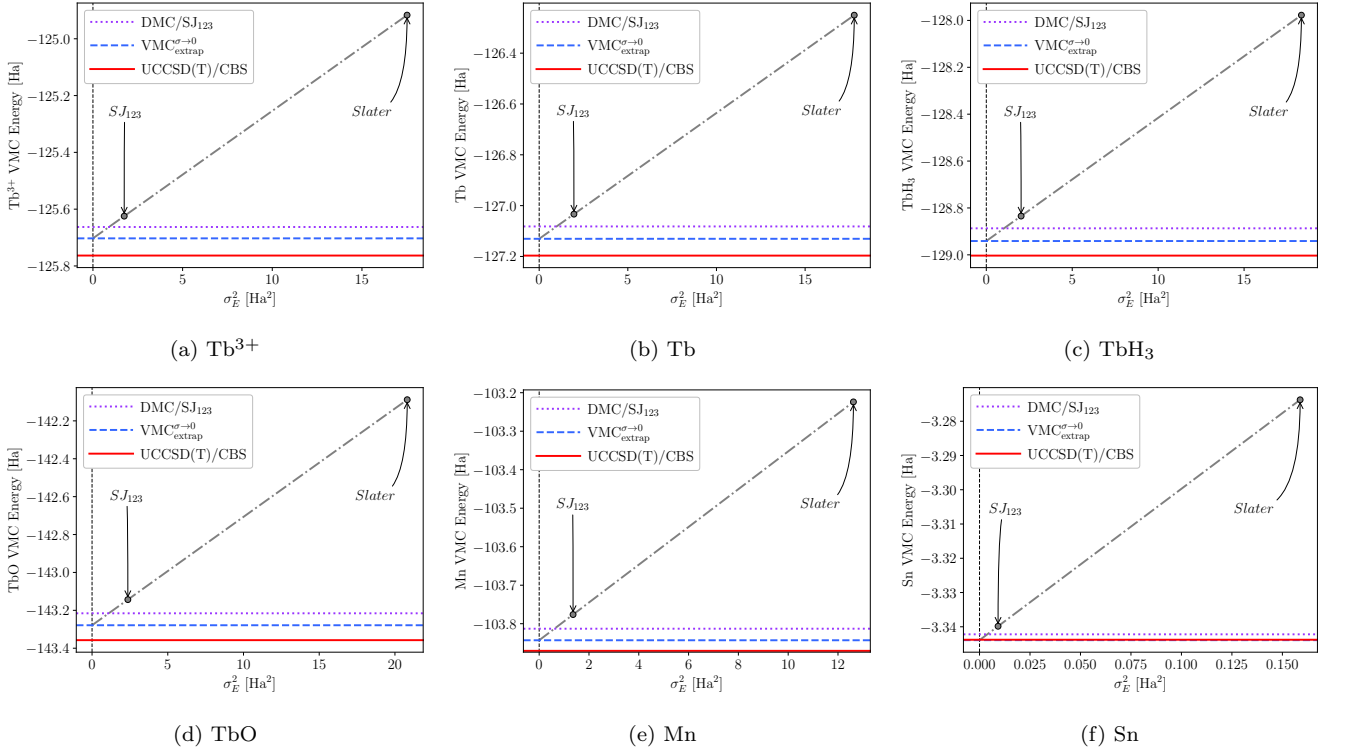


FIG. 26: VMC energy vs. variance extrapolations for molecular systems relevant for TbMn_6Sn_6 .

TABLE 18: Estimation of combined FN and localization biases in single-reference DMC calculations for TbMn_6Sn_6 relevant systems. Total energies [Ha] using various methods are shown. Uncontracted aug-cc-p(wC)VnZ basis sets were used in the extrapolations with $nZ \in (\text{DZ-QZ})$ for Tb systems and $nZ \in (\text{TZ-5Z})$ for Sn and Mn atoms. 0.001 Ha^{-1} timestep and aug-cc-pVTZ basis sets were used in all DMC calculations. In DMC, T-moves [119] and locality-approximation (LA) [120] algorithms are used for evaluating non-local ECPs. Var/Energy [Ha] is the DMC/ROHF (T-moves) variance to energy ratio. ϵ [mHa] represents the DMC/ROHF (T-moves) error compared to UCCSD(T)/CBS, $\epsilon = (E_{DMC} - E_{exact})$. η is the missing percentage of the correlation energy $\eta = 100\% \cdot \epsilon/|E_{corr}|$. SCF calculations are of spin-restricted type, ROHF or RKS.

Method	NL-Eval	Tb ³⁺	Tb	TbH ₃	TbO	Mn	Sn
ROHF/CBS		-124.9172	-126.2515	-127.9783	-142.0898	-103.2242	-3.2736
UCCSD(T)/CBS		-125.7634	-127.1967	-129.0033	-143.3574	-103.8704	-3.3438
DMC/HF	T-moves	-125.6628(3)	-127.0819(3)	-128.8869(4)	-143.2157(6)	-103.8130(4)	-3.3422(1)
DMC/PBE0	T-moves	-125.6537(3)	-127.0723(3)	-128.8769(6)	-143.2109(5)	-103.8162(3)	-3.3424(1)
DMC/PBE	T-moves	-125.6478(3)	-127.0651(3)	-128.8705(4)	-143.2027(5)	-103.8163(3)	-3.3425(1)
DMC/HF	LA	-125.6829(4)	-127.1054(4)	-128.9105(7)	-143.2500(5)	-103.8166(3)	-3.3435(1)
DMC/PBE0	LA	-125.6740(4)	-127.0979(4)	-128.9041(5)	-143.2489(6)	-103.8204(3)	-3.3435(1)
DMC/PBE	LA	-125.6696(4)	-127.0914(4)	-128.8979(5)	-143.2403(6)	-103.8206(4)	-3.3434(1)
Var/Energy [Ha]	T-moves	0.014375(6)	0.015376(8)	0.01560(2)	0.01673(2)	0.01313(1)	0.00341(3)
ϵ [mHa]	T-moves	100.6(3)	114.8(3)	116.4(4)	141.7(6)	57.4(4)	1.6(1)
η [%]	T-moves	11.89(4)	12.14(3)	11.35(4)	11.18(5)	8.89(6)	2.3(1)

TABLE 19: Experimental bulk geometry of TbMn_6Sn_6 [23].
 $a = 5.530(1) \text{ \AA}$, $c = 9.023(2) \text{ \AA}$.

Atom	Position	Symmetry	x	y	z
Tb	1(b)	$6/mmm$	0	0	1/2
Mn	6(i)	mm	1/2	0	0.2525(2)
Sn ₁	2(e)	$6mm$	0	0	0.1624(1)
Sn ₂	2(d)	$\bar{6}2m$	1/3	2/3	1/2
Sn ₃	2(c)	$\bar{6}2m$	1/3	2/3	0

TABLE 20: Experimental bulk geometry of TbMn_6Sn_6 in XSF format (Angstrom units).

CRYSTAL			
PRIMVEC			
	4.7891204829	-2.7650000000	0.0000000000
	0.0000000000	5.5300000000	0.0000000000
	0.0000000000	0.0000000000	9.0230000000
PRIMCOORD			
13	1		
65	0.0000000000	0.0000000000	-4.5115000000
25	2.3945602415	1.3825000000	2.2783075000
25	-2.3945602415	1.3825000000	2.2783075000
25	0.0000000000	-2.7650000000	2.2783075000
25	2.3945602415	1.3825000000	-2.2783075000
25	-2.3945602415	1.3825000000	-2.2783075000
25	-0.0000000000	-2.7650000000	-2.2783075000
50	0.0000000000	0.0000000000	1.4653352000
50	-3.1927469886	-0.0000000000	-4.5115000000
50	-3.1927469886	-0.0000000000	0.0000000000
50	0.0000000000	0.0000000000	-1.4653352000
50	-1.5963734943	2.7650000000	4.5115000000
50	-1.5963734943	2.7650000000	0.0000000000

TABLE 21: Employed slab geometry of TbMn₆Sn₆ in XSF format (Angstrom units).

CRYSTAL			
PRIMVEC			
	4.7891204829	-2.7650000000	0.0000000000
	0.0000000000	5.5300000000	0.0000000000
	0.0000000000	0.0000000000	27.0690000000
PRIMCOORD			
23 1			
65	0.0000000000	0.0000000000	13.5345000000
25	2.3945602415	-1.3825000000	-6.7446925000
25	2.3945602415	-4.1475000000	-6.7446925000
25	0.0000000000	-2.7650000000	-6.7446925000
25	2.3945602415	-1.3825000000	-11.3013075000
25	2.3945602415	1.3825000000	-11.3013075000
25	-0.0000000000	-2.7650000000	-11.3013075000
25	2.3945602415	-1.3825000000	11.3013075000
25	2.3945602415	-4.1475000000	11.3013075000
25	0.0000000000	-2.7650000000	11.3013075000
25	2.3945602415	-1.3825000000	6.7446925000
25	2.3945602415	1.3825000000	6.7446925000
25	-0.0000000000	-2.7650000000	6.7446925000
50	0.0000000000	0.0000000000	10.4883352000
50	0.0000000000	0.0000000000	-7.5576648000
50	0.0000000000	0.0000000000	7.5576648000
50	0.0000000000	0.0000000000	-10.4883352000
50	1.5963734943	-2.7650000000	13.5345000000
50	-1.5963734943	2.7650000000	13.5345000000
50	1.5963734943	-2.7650000000	9.0230000000
50	1.5963734943	-2.7650000000	-9.0230000000
50	-1.5963734943	2.7650000000	9.0230000000
50	-1.5963734943	2.7650000000	-9.0230000000